

DRAFT VERSION SEPTEMBER 4, 2024
Typeset using L^AT_EX **modern** style in AASTeX63

The densities in diffuse and translucent molecular clouds: estimates from observations of C₂ and from 3-dimensional extinction maps

DAVID A. NEUFELD,¹ DANIEL E. WELTY,² ALEXEI V. IVLEV,³ PAOLA CASELLI,³
GORDIAN EDENHOFER,⁴ NICK INDRIOLO,⁵ MARTA OBOLENTSEVA,³
KEDRON SILSBEE,⁶ PAULE SONNENTRUCKER,⁷ AND MARK G. WOLFIRE⁸

¹*William H. Miller Department of Physics & Astronomy, Johns Hopkins University, Baltimore, MD 21218, USA*

²*Space Telescope Science Institute, Baltimore, MD 21218, USA*

³*Max-Planck Institute for Extraterrestrial Physics, 85748 Garching, DE*

⁴*Max Planck Institute for Astrophysics, 85748 Garching, DE*

⁵*AURA for ESA, Space Telescope Science Institute, Baltimore, MD 21218, USA*

⁶*University of Texas, El Paso, TX 79968, USA*

⁷*European Space Agency, ESA office at STScI, Baltimore, MD 21218, USA*

⁸*University of Maryland, College Park, MD 20742, USA*

ABSTRACT

Newly-computed collisional rate coefficients for the excitation of C₂ in collisions with H₂, presented recently by Najar and Kalugina (2020), are significantly larger than the values adopted previously in models for the excitation of the C₂ molecule, a widely used probe of the interstellar gas density. With these new rate coefficients, we have modeled the C₂ rotational distributions inferred from visible and ultraviolet absorption observations of electronic transitions of C₂ towards a collection of 46 nearby background sources. The inferred gas densities in the foreground interstellar clouds responsible for the observed C₂ absorption are a factor 4 to 7 smaller than those inferred previously, a direct reflection of the larger collisional rate coefficients computed by Najar and Kalugina (2020). These lower density estimates are generally in good agreement with the peak densities inferred from 3D extinction maps for the relevant sightlines. In cases where H₃⁺ absorption has also been observed and used to estimate the cosmic-ray ionization rate (CRIR), our estimates of the latter will also decrease accordingly because the H₃⁺ abundance is a function of the ratio of the CRIR to the gas density.

Keywords: Galactic cosmic rays (567), Diffuse molecular clouds (381), Interstellar molecules (849)

Corresponding author: David A. Neufeld

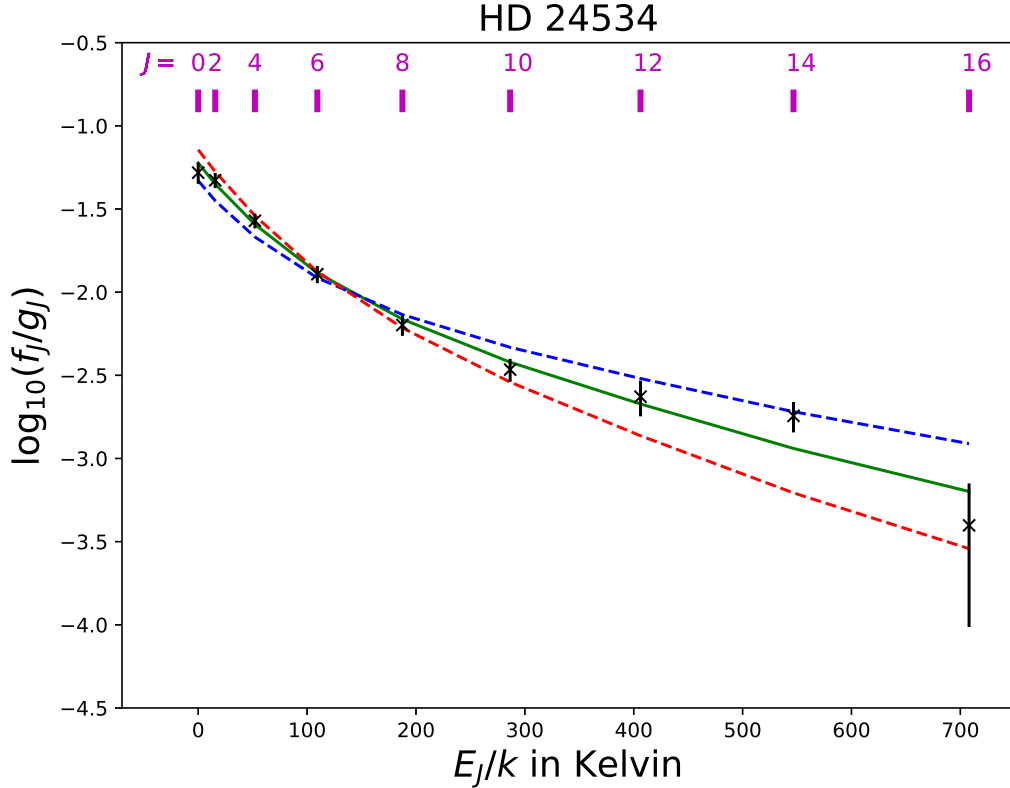


Figure 1. Rotational diagram from C_2 absorption line observations (S07) toward HD 24534. Green curve: best fit, obtained for $T = 48$ K and $n_H = 70 \text{ cm}^{-3}$, using the excitation model described in Section 3. Red dashed curve: fit for $T = 48$ K and $n_H = 98 \text{ cm}^{-3}$. Blue dashed curve: fit for $T = 48$ K and $n_H = 50 \text{ cm}^{-3}$.

1. INTRODUCTION

The diatomic carbon molecule, C_2 , has been widely used as a density estimator in the diffuse and translucent interstellar clouds. As discussed by Chaffee et al. (1980) and van Dishoeck & Black (1982; hereafter vDB82), the rotational distribution of C_2 in its ground vibrational and electronic state – which can be measured by means of absorption line observations of several electronic bands in the visible and ultraviolet spectral regions – reflects a competition between inelastic collisions with He or H_2 and pumping by the interstellar radiation field (ISRF), primarily in the Phillips A – X band near $1 \mu\text{m}$. Figure 1 shows an example rotational diagram obtained toward the star HD 24534 (Sonnentrucker et al. 2007; hereafter S07), in which $\log_{10}(f_J/g_J)$ is plotted against E_J/k , where f_J is the fractional population in the state of rotational quantum number, J , and E_J and $g_J = 2J + 1$ are the energy and degeneracy of that state. For C_2 , only even- J states are present because the wavefunction must be symmetric under exchange of the two identical (bosonic) nuclei. For low J , the populations are controlled by collisional excitation, and the (negative) slope of the rotational diagram is inversely proportional to the kinetic temperature of the gas.

For high J , the effects of radiative pumping become important, and the slope of the curve becomes less negative. The value of E_J above which the slope becomes less negative is accordingly an increasing function of density. The green curve is a best fit to the observed data, obtained using the methods described in Section 3 below for a gas kinetic temperature, $T = 48$ K, and a gas density, $n_{\text{H}} = 70 \text{ cm}^{-3}$, defined here as the volume density of hydrogen nuclei, $n(\text{H}) + n(\text{H}^+) + 2n(\text{H}_2)$. Red and blue curves show respectively the rotational diagrams expected for assumed densities that are 40% larger and 40% smaller than the best-fit values.

Following Chaffee et al. (1980), and in the absence of any quantum-mechanical calculations of relevance, vDB82 adopted a very simple approximation for the excitation rates for C_2 . They assumed that the collisional cross-section, $\sigma(2,0)$, for de-excitation from $J = 2$ to $J = 0$ was $2 \times 10^{-16} \text{ cm}^2$ independent of energy. For other collisionally-induced deexcitations from J_u to J_l , they adopted a cross-section $\sigma(J_u, J_l) = 5\sigma(2,0)/(2J_u + 1)$ for $J_u = J_l + 2$ and $\sigma(J_u, J_l) = 0$ otherwise. They also computed the radiative excitation matrix, $Y(J_i, J_f)$, which describes the probability that radiative pumping in an initial rotational state J_i will be followed by a radiative cascade that ultimately leads to a reentry into the ground electronic and vibrational state in rotational state J_f . Together with an estimate of the pumping rate, W_J , (dependent on the ISRF and the relevant oscillator strengths) and the inclusion of spontaneous radiative decay within the ground vibrational state (generally negligible because the pure rotational transitions are dipole-forbidden), this allowed vDB82 to compute the fractional level populations of C_2 , f_J , expected in equilibrium, as a function of density and temperature.

Over the subsequent four decades, the treatment of C_2 excitation described by vDB82 has been widely used to determine densities in the interstellar medium and has been implemented in an online tool. Because vDB82 adopted the same collisional excitation rates for excitation by all collision partners (e.g. H, H_2 and He), the densities thereby determined were considered to be the total particle densities, $n = n(\text{H}) + n(\text{H}_2) + n(\text{He})$. Casu and Cecchi-Pestellini (2012, hereafter CC12) presented the results from a revised excitation model in which the radiative excitation matrix and pumping rate were recomputed to reflect recent improvements in the molecular data and the collisional rate coefficients were updated beyond the simple estimates introduced by Chaffee et al. (1980). Here, they made use of close-coupling calculations of the rate coefficients for excitation of C_2 by He (Najar et al. 2008) and para- H_2 (Najar et al. 2009). As discussed in Section 2, a recent high-accuracy calculation of the rate coefficients for excitation of C_2 by both ortho- and para- H_2 (Najar & Kalugina 2020, hereafter NK20) allows the use of C_2 as a density estimator to be placed on a sounder footing and leads to a significant decrease in the inferred gas densities.

With the advent of high-quality observational data obtained with *Gaia*, an alternative method of density estimation has emerged. Distance and G-band extinction

measurements have been obtained toward a large sample of stars in the Galaxy, allowing 3-dimensional maps of the extinction density (i.e. extinction per unit path length) to be constructed (e.g. Lallement et al. 2019; Leike et al. 2020, hereafter L20; Edenhofer et al. 2023, hereafter E23). For a given assumed gas-to-extinction ratio, these maps may be used to determine the gas density, n_{H} , on a 3-dimensional grid of Galactic positions (X, Y, Z) . In Section 3, we discuss the comparison between the density estimates obtained from the 3D extinction maps with those obtained using our updated analysis of C_2 absorption spectra: results are given for 23 sightlines toward background sources located within 1.25 kpc of the Sun. In section 4, we discuss briefly the implications of our lower density estimates in translucent interstellar clouds for the cosmic-ray ionization rates (CRIR) inferred from observations of H_3^+ . A more sophisticated analysis, performed with the use of models that account for the observed 3D distribution of gas and hot stars, is presented in a companion paper by Obolentseva et al. (2024).

2. C_2 DENSITY ESTIMATES

Our treatment of the excitation of C_2 follows closely the methodology of vDB82. We solve the equations of statistical equilibrium (vDB82, equation 27) as a function of gas kinetic temperature and density, but we use the collisional rate coefficients computed by NK20 in place of the simple formula introduced by Chaffee et al. (1980). Figure 2 shows a comparison of the rate coefficients for collisional deexcitation to the ground state ($J = 0$) from the first excited rotational state ($J = 2$).

The black curve shows the value adopted by vDB82. The red and blue curves show the NK20 results for collisions with para- H_2 and ortho- H_2 respectively, and the magenta curve shows the earlier results obtained for He (Najar et al. 2008). As noted by NK20, the rate coefficient for excitation by ortho- H_2 is much larger than that for para- H_2 , a behavior that is observed in many other systems. Thus, the availability of the new NK20 rate coefficients with their first high-quality calculation for excitation by ortho- H_2 has a significant impact on our understanding of C_2 excitation. The cyan curve shows the weighted average appropriate to an H_2 ortho-to-para ratio in equilibrium at the gas kinetic temperature. The green curve includes the additional effect due to He for an assumed He abundance of 0.2 relative to H_2 , and is defined such that the total deexcitation rate per C_2 molecule, including the effects of helium, is $q(2, 0)n(\text{H}_2)$.

Moreover, while the cross-sections $\sigma(J_u, J_u - 2)$ adopted by vDB82 are a monotonically decreasing function of J_u , the values of $\sigma(4, 2)$ computed by NK20 are larger than those for $\sigma(2, 0)$, a behavior noted in previous studies (e.g. Phillips 1994). Figure 3 shows the ratio $q(J_u, J_u - 2)/q(2, 0)$ computed by NK20 at a temperature of 60 K, both for collisions with para- H_2 (red) and ortho- H_2 (blue). For comparison, the dependence assumed by vDB82 is shown by the black curve.

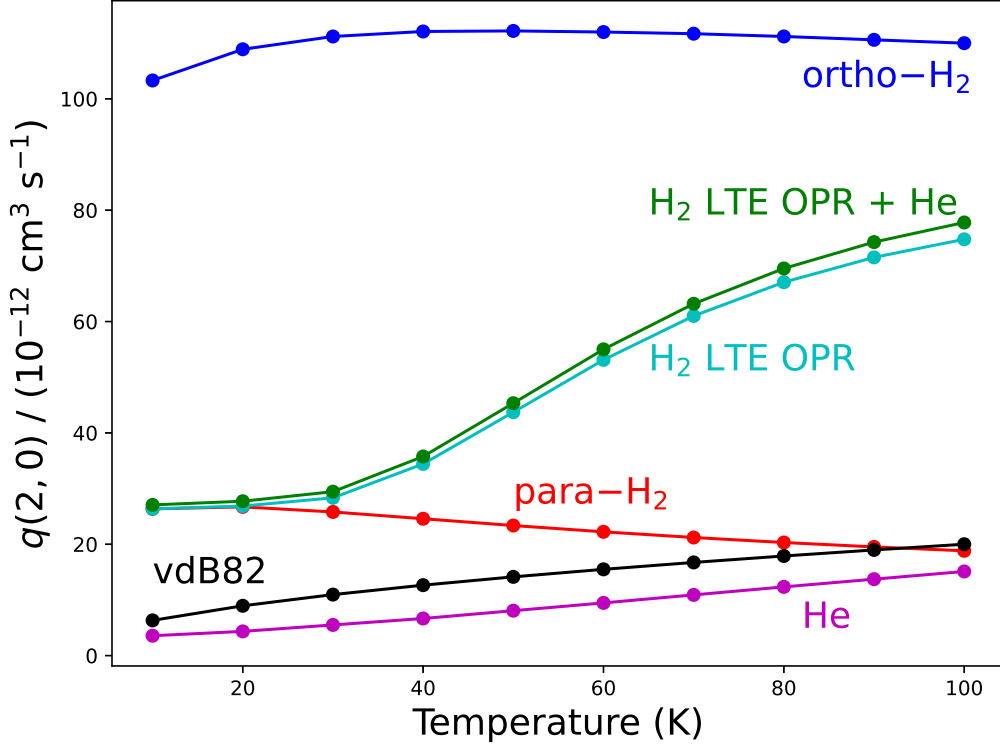


Figure 2. Comparison of rate coefficients for the collisional de-excitation of C_2 $J = 2$ to $J = 0$ computed for various collision partners: para- H_2 (from NK20 in red), ortho- H_2 (from NK20 in blue), and He (from Najjar et al. 2008 in magenta). Cyan points: weighted average of NK20 results for an H_2 ortho-to-para ratio in LTE. Green points: weighted averaged per H_2 molecule, including the additional contribution of He for a He/ H_2 abundance ratio of 0.2. Black points: simple expression adopted by vDB82.

We have also adopted the revised radiative excitation matrix, $Y(J_i, J_f)$, recomputed by CC12 for the ISRF assumed by vDB82 and given by:

$$\frac{4\pi J_\nu}{h\nu} = 1.54 \times 10^{-5} \lambda_{\mu m}^{2.7} \text{ photons cm}^{-2} \text{ s}^{-1} \text{ Hz}^{-1}, \quad (1)$$

where J_ν is the mean (angle averaged) intensity at frequency ν , and $\lambda_{\mu m}$ is the wavelength in micron.

Over the $0.77 - 1.21 \mu m$ range most relevant for C_2 excitation, the $\lambda_{\mu m}^{2.7}$ wavelength dependence adopted by vDB82 is in excellent agreement with a subsequent study of the ISRF by Mathis et al. (1983). However, the absolute value of the ISRF adopted by vDB82 is a factor¹ 1.39 smaller than that measured ($0.496 \text{ MJy sr}^{-1}$) by the DIRBE instrument on *COBE* at $1.25 \mu m$ (Hauser et al. 1998). Accordingly, we have scaled

¹ In determining this factor, we made use of the zodi-subtracted DIRBE all-sky map, available in an equal area pixelation (HEALPix) at https://irsa.ipac.caltech.edu/data/Planck/release_1/external-data/external_maps.html, and the DIRBE Band 1 spectral response function at https://lambda.gsfc.nasa.gov/product/cobe/dirbe_ancil_sr_get.html

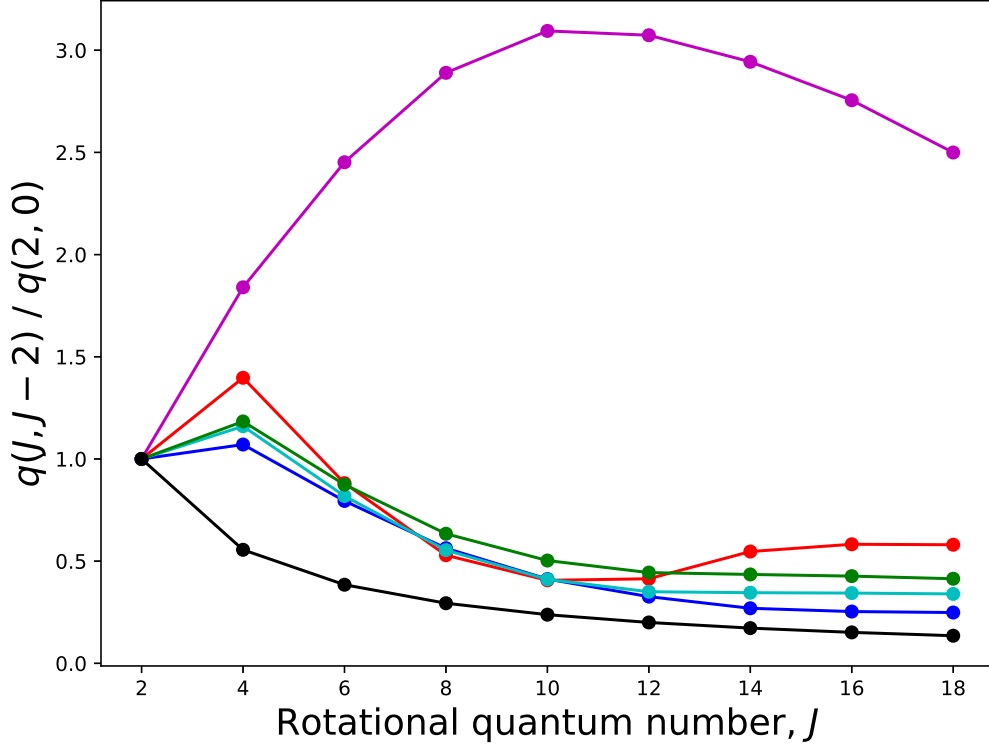


Figure 3. The ratio $q(J_u, J_u - 2)/q(2, 0)$ computed by NK20 at a temperature of 60 K, both for collisions with para-H₂ (red), ortho-H₂ (blue), and He (magenta). Cyan points: weighted average of NK20 results for an H₂ ortho-to-para ratio in LTE. Green points: weighted averaged per H₂ molecule, including the additional contribution of He for a He/H₂ abundance ratio of 0.2. Black points: dependence assumed by vDB82.

the pumping rate given by CC12 ($W_J = 3.1 \times 10^{-9} \text{ s}^{-1}$, independent of J) by a factor 1.39 to obtain the revised estimate $W_J = 4.3 \times 10^{-9} \text{ s}^{-1}$.

We have used our C₂ excitation model to fit the fractional C₂ populations, f_J , obtained from absorption line spectroscopy performed toward 46 background sources for which C₂ has been detected in rotational states extending up to $J = 12$ or higher: estimates of f_J with $J \geq 12$ are needed to provide enough leverage on the rotational diagram to constrain the gas density. Our sample – listed in Table 1 – was assembled from a combination of previously-published results and fits to archival data. The latter were downloaded from the relevant archive and their spectra normalized to the continuum. We then performed profile fits to the normalized spectra, using the wavelengths and oscillator strengths adopted by S07. The Doppler parameter, b , was assumed to be the same for all transitions, with a value of 1 km s^{-1} being typically adopted. The derived column densities show little dependence on the value of b , because the lines are typically optically-thin. In most cases, all the lines were fitted simultaneously with a single component. In cases where C₂ was not detected in rotational states as high as $J = 12$, the model typically yields little useful information:

only lower limits on the density are obtained, and these typically lie below the values obtained for other sources where states of $J \geq 12$ are available.

In Figure 4, example results are shown for the sightline toward HD 24534. Here, we present contours of χ^2 in the plane of gas density, n_{H} , and kinetic temperature, T . Blue contours show the results obtained with the new NK20 collision rate coefficients, and red contours are those obtained with the collisional cross-sections used by vDB82. Blue and red dots show the best-fit values in each case, and the three contours of each color show the 1, 2, and 3 σ error ellipses. These were obtained by scaling the stated observational errors to yield a minimum χ^2 equal to the number of degrees of freedom, and then plotting contours of constant χ^2 equal to that minimum value plus 1, 4, and 9. The two fits are equally good, with reduced χ^2 values of 1.29 and 1.28 respectively, but the best-fit densities differ by a factor of 7.8.

As expected given the collisional cross-sections shown in Figure 2, the derived gas densities with the NK20 rate coefficients are dramatically lower than those obtained with the vDB82 estimates; the temperatures, by contrast, are almost identical because they simply reflect the slope of the rotational diagram for small J . The blue points in Figure 5 show the ratio of the densities obtained with the vDB82 estimates to those obtained with the NK20 rate coefficients. Results are shown here as a function of the inferred gas temperature (obtained with the vDB rates).

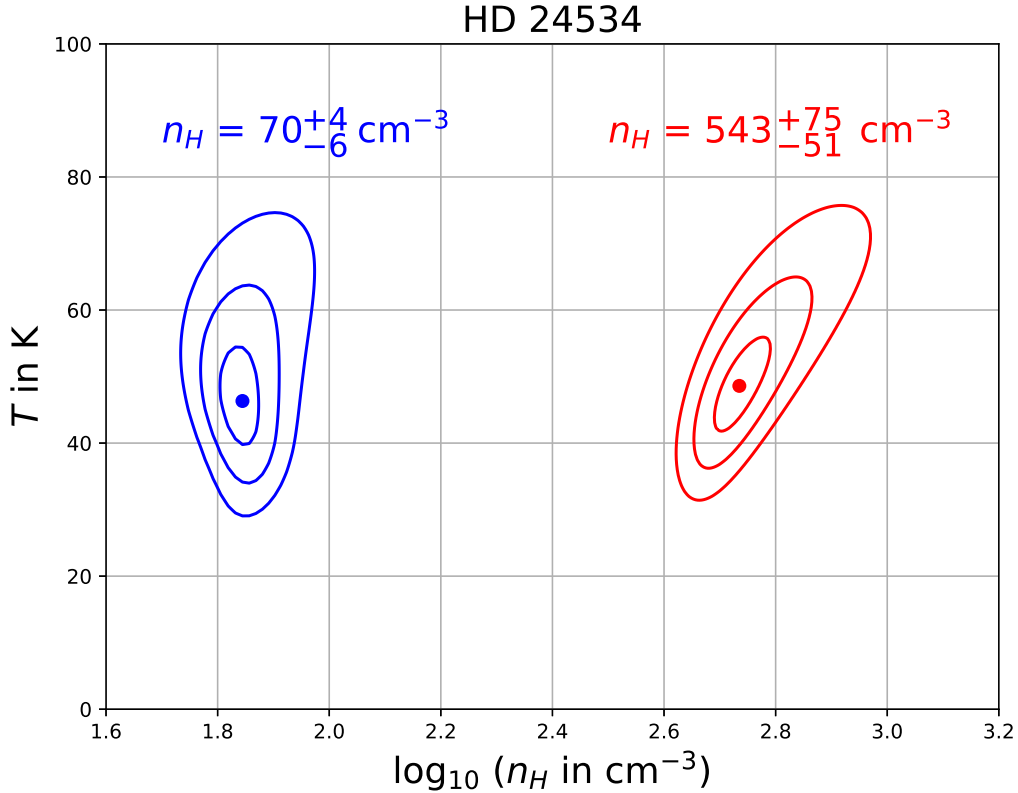


Figure 4. Contours of constant χ^2 in the plane of gas density, n_{H} , and kinetic temperature, T , for the fit to the C_2 rotational diagram observed toward HD 24534. Blue: 1 σ , 2 σ , and 3 σ error ellipses

Table 1. C₂ column densities (10¹³ cm⁻²), and derived temperatures (K) and densities (cm⁻³)

Source	N(0)	N(2)	N(4)	N(6)	N(8)	N(10)	N(12)	N(14)	N(16)	N(18)	$n_{\text{H}}(\text{C}_2)$	$T(\text{C}_2)$	Ref ^a
Cernis 52	0.88 ± 0.13	2.79 ± 0.30	2.54 ± 0.32	1.54 ± 0.22	0.98 ± 0.38	0.66 ± 0.29	0.63 ± 0.21	94 ⁺⁶ ₋₆	32 ⁺⁵ ₋₅	IG11
HD 24534	0.16 ± 0.02	0.72 ± 0.06	0.74 ± 0.06	0.51 ± 0.05	0.33 ± 0.04	0.22 ± 0.03	0.18 ± 0.04	0.16 ± 0.03	0.04 ± 0.03	...	70 ⁺⁴ ₋₆	46 ⁺⁹ ₋₇	S07
HD 27778	0.15 ± 0.02	0.59 ± 0.05	0.62 ± 0.05	0.52 ± 0.04	0.34 ± 0.04	0.18 ± 0.03	0.15 ± 0.02	0.11 ± 0.02	0.09 ± 0.02	0.06 ± 0.02	64 ⁺² ₋₄	50 ⁺⁸ ₋₆	S07
HD 29647	2.08 ± 0.04	3.68 ± 0.05	1.79 ± 0.05	0.82 ± 0.04	0.65 ± 0.05	0.63 ± 0.11	0.54 ± 0.05	122 ⁺⁸ ₋₆	10 ⁺² ₋₁	ARC
HD 34078	0.24 ± 0.02	1.05 ± 0.04	1.23 ± 0.04	1.22 ± 0.04	0.98 ± 0.04	0.75 ± 0.04	0.60 ± 0.04	...	0.22 ± 0.05	...	56 ⁺²⁸ ₋₁₀	97 ⁺²⁶ ₋₁₉	ARC
NGC2024 1	1.22 ± 0.07	4.09 ± 0.12	4.05 ± 0.13	2.43 ± 0.12	1.58 ± 0.12	1.08 ± 0.11	0.43 ± 0.12	0.50 ± 0.12	96 ⁺⁶ ₋₄	41 ⁺⁴ ₋₄	ARC
HD 46202	0.10 ± 0.02	0.47 ± 0.04	0.43 ± 0.04	0.37 ± 0.03	0.28 ± 0.03	0.14 ± 0.03	0.11 ± 0.05	80 ⁺³⁶ ₋₁₂	64 ⁺¹⁷ ₋₁₄	STIS
HD 46223	0.09 ± 0.02	0.34 ± 0.03	0.38 ± 0.03	0.35 ± 0.03	0.19 ± 0.03	0.09 ± 0.03	0.07 ± 0.03	164 ⁺⁷⁷³ ₋₆₂	84 ⁺¹⁷ ₋₁₃	STIS
Walker 67	0.43 ± 0.01	1.50 ± 0.01	1.26 ± 0.01	0.79 ± 0.01	0.45 ± 0.01	0.27 ± 0.01	0.21 ± 0.01	0.21 ± 0.01	102 ⁺⁶ ₋₄	33 ⁺⁴ ₋₃	UVG
HD 62542	0.69 ± 0.05	2.58 ± 0.14	2.57 ± 0.14	1.63 ± 0.08	0.85 ± 0.04	0.48 ± 0.03	0.29 ± 0.03	0.20 ± 0.02	0.10 ± 0.02	0.10 ± 0.02	104 ⁺⁶ ₋₄	41 ⁺⁵ ₋₅	W20
HD 63804	0.48 ± 0.02	1.91 ± 0.03	1.73 ± 0.07	1.27 ± 0.03	0.88 ± 0.03	0.50 ± 0.03	0.38 ± 0.03	0.33 ± 0.06	82 ⁺⁴ ₋₂	42 ⁺⁵ ₋₄	UVG
HD 73882	0.71 ± 0.06	1.56 ± 0.09	0.81 ± 0.05	0.46 ± 0.04	0.21 ± 0.03	0.13 ± 0.03	0.12 ± 0.03	0.09 ± 0.03	0.05 ± 0.03	...	132 ⁺¹⁰ ₋₈	16 ⁺³ ₋₃	STIS
HD 80077	0.96 ± 0.21	3.23 ± 0.46	1.77 ± 0.54	1.23 ± 0.49	0.84 ± 0.42	0.94 ± 0.50	0.73 ± 0.42	88 ⁺¹² ₋₈	20 ⁺⁵ ₋₄	G99
HD 112272	0.06 ± 0.02	0.23 ± 0.02	0.17 ± 0.02	0.27 ± 0.02	0.24 ± 0.02	0.12 ± 0.02	0.21 ± 0.02	78 ⁺⁹²³ ₋₅₀	156 ⁺⁴⁸ ₋₁₃₈	UVP
HD 136239	0.28 ± 0.04	0.93 ± 0.08	0.73 ± 0.13	0.57 ± 0.12	0.25 ± 0.12	0.17 ± 0.06	0.13 ± 0.07	0.10 ± 0.09	104 ⁺⁶ ₋₆	33 ⁺⁵ ₋₄	K10
HD 147084	0.19 ± 0.06	0.76 ± 0.15	0.70 ± 0.23	0.58 ± 0.15	0.57 ± 0.13	0.24 ± 0.14	0.23 ± 0.14	0.17 ± 0.13	62 ⁺⁸ ₋₈	50 ⁺²⁰ ₋₁₄	vDB
HD 147888	0.10 ± 0.02	0.33 ± 0.03	0.36 ± 0.03	0.30 ± 0.03	0.18 ± 0.03	0.14 ± 0.02	0.08 ± 0.02	0.05 ± 0.02	68 ⁺⁴ ₋₂	56 ⁺⁹ ₋₇	S07
HD 147889	0.86 ± 0.03	2.71 ± 0.04	2.85 ± 0.05	2.29 ± 0.04	1.59 ± 0.05	0.93 ± 0.07	0.69 ± 0.04	0.31 ± 0.04	0.14 ± 0.03	...	72 ⁺⁴ ₋₂	54 ⁺⁷ ₋₆	ARC
HD 147933	0.12 ± 0.01	0.52 ± 0.02	0.52 ± 0.02	0.30 ± 0.02	0.20 ± 0.02	0.15 ± 0.02	0.08 ± 0.02	0.05 ± 0.02	0.05 ± 0.02	0.04 ± 0.02	84 ⁺⁶ ₋₄	43 ⁺⁵ ₋₅	STIS
HD 148184	0.18 ± 0.02	0.70 ± 0.03	0.81 ± 0.04	0.63 ± 0.04	0.39 ± 0.04	0.34 ± 0.03	0.14 ± 0.07	78 ⁺³⁰ ₋₁₂	65 ⁺¹⁶ ₋₁₄	UVP
HD 148379	0.07 ± 0.04	0.25 ± 0.07	0.24 ± 0.09	0.21 ± 0.09	0.15 ± 0.08	0.11 ± 0.10	0.06 ± 0.05	70 ⁺⁴ ₋₆	48 ⁺¹² ₋₉	K10
HD 149757	0.08 ± 0.01	0.26 ± 0.02	0.32 ± 0.03	0.25 ± 0.03	0.18 ± 0.03	0.14 ± 0.02	0.11 ± 0.02	0.08 ± 0.02	0.06 ± 0.02	...	52 ⁺² ₋₂	48 ⁺⁶ ₋₆	S07
HD 151932	0.20 ± 0.04	0.54 ± 0.09	0.56 ± 0.08	0.48 ± 0.10	0.20 ± 0.10	0.24 ± 0.09	0.16 ± 0.14	0.10 ± 0.08	76 ⁺⁶ ₋₈	37 ⁺¹¹ ₋₉	K10
HD 152003	0.08 ± 0.02	0.43 ± 0.03	0.47 ± 0.03	0.42 ± 0.03	0.30 ± 0.03	0.26 ± 0.03	0.23 ± 0.07	58 ⁺²² ₋₈	74 ⁺²³ ₋₁₇	UVP
HD 152235	0.12 ± 0.02	0.41 ± 0.04	0.31 ± 0.03	0.35 ± 0.03	0.23 ± 0.03	0.15 ± 0.03	0.17 ± 0.03	64 ⁺¹⁰ ₋₁₄	35 ⁺²⁸ ₋₁₃	UVP
HD 152236	0.13 ± 0.03	0.36 ± 0.06	0.30 ± 0.06	0.29 ± 0.06	0.13 ± 0.06	0.12 ± 0.10	0.08 ± 0.07	86 ⁺¹⁴ ₋₁₀	32 ⁺¹³ ₋₉	K10

Table 1 (contd.). C₂ column densities (10^{13} cm^{-2}), and derived temperatures (K) and densities (cm^{-3})

Source	N(0)	N(2)	N(4)	N(6)	N(8)	N(10)	N(12)	N(14)	N(16)	N(18)	$n_{\text{H}}(\text{C}_2)$	$T(\text{C}_2)$	Ref ^a
HD 152270	0.10 ± 0.02	0.28 ± 0.03	0.39 ± 0.03	0.29 ± 0.04	0.13 ± 0.04	0.16 ± 0.04	0.11 ± 0.08	82^{+138}_{-18}	68^{+28}_{-19}	UVP
HD 152590	0.07 ± 0.01	0.24 ± 0.02	0.25 ± 0.02	0.17 ± 0.02	0.10 ± 0.02	0.08 ± 0.02	0.05 ± 0.02	88^{+6}_{-6}	46^{+6}_{-5}	STIS
HD 154368	0.41 ± 0.02	1.33 ± 0.05	1.16 ± 0.06	0.83 ± 0.06	0.64 ± 0.06	0.32 ± 0.06	0.18 ± 0.05	0.29 ± 0.08	0.27 ± 0.08	...	80^{+4}_{-4}	33^{+5}_{-5}	K10
HD 163800	0.19 ± 0.03	0.49 ± 0.06	0.64 ± 0.09	0.47 ± 0.09	0.27 ± 0.07	0.19 ± 0.08	...	0.13 ± 0.09	78^{+46}_{-12}	52^{+22}_{-17}	K09
HD 169454	0.95 ± 0.04	2.38 ± 0.06	1.48 ± 0.05	0.68 ± 0.05	0.40 ± 0.05	0.18 ± 0.05	0.18 ± 0.05	0.12 ± 0.08	0.12 ± 0.08	...	136^{+8}_{-8}	21^{+2}_{-2}	K09
HD 170740	0.24 ± 0.10	0.41 ± 0.06	0.42 ± 0.06	0.22 ± 0.07	0.32 ± 0.10	0.13 ± 0.05	0.14 ± 0.05	70^{+10}_{-8}	31^{+15}_{-12}	K10
HD 172028	1.00 ± 0.04	2.97 ± 0.06	2.58 ± 0.07	1.86 ± 0.06	1.14 ± 0.06	0.64 ± 0.13	0.32 ± 0.06	0.50 ± 0.07	94^{+6}_{-6}	35^{+5}_{-5}	ARC
HD 179406	0.24 ± 0.02	1.03 ± 0.03	1.17 ± 0.04	0.88 ± 0.04	0.37 ± 0.03	0.20 ± 0.07	0.12 ± 0.04	0.14 ± 0.05	162^{+326}_{-50}	68^{+12}_{-10}	ARC
HD 229059	0.28 ± 0.09	1.14 ± 0.17	1.27 ± 0.20	1.10 ± 0.03	0.72 ± 0.06	0.60 ± 0.05	0.29 ± 0.03	0.25 ± 0.03	0.26 ± 0.04	...	58^{+4}_{-4}	65^{+12}_{-10}	ARC
CygOB2 5	0.47 ± 0.06	1.82 ± 0.09	2.62 ± 0.15	1.72 ± 0.10	1.13 ± 0.11	0.73 ± 0.10	0.53 ± 0.10	84^{+42}_{-16}	71^{+15}_{-13}	HIR
CygOB2 12	1.64 ± 0.03	5.37 ± 0.04	5.31 ± 0.13	3.64 ± 0.05	2.55 ± 0.05	1.59 ± 0.04	1.04 ± 0.04	0.51 ± 0.04	82^{+2}_{-1}	40^{+4}_{-3}	ARC
HD 203532	0.22 ± 0.06	0.98 ± 0.16	0.89 ± 0.14	0.60 ± 0.13	0.39 ± 0.12	0.45 ± 0.13	0.30 ± 0.11	70^{+8}_{-8}	37^{+11}_{-8}	HSF
HD 203938	0.21 ± 0.03	0.50 ± 0.04	0.70 ± 0.05	0.63 ± 0.05	0.55 ± 0.05	0.24 ± 0.05	0.47 ± 0.10	60^{+412}_{-16}	88^{+56}_{-34}	ARC
HD 204827	1.76 ± 0.15	5.63 ± 0.15	5.06 ± 0.15	3.38 ± 0.15	1.80 ± 0.15	0.78 ± 0.15	0.64 ± 0.15	0.51 ± 0.06	0.24 ± 0.04	...	102^{+6}_{-4}	38^{+5}_{-4}	ARC
HD 206267	0.41 ± 0.02	1.23 ± 0.03	1.07 ± 0.03	0.58 ± 0.02	0.31 ± 0.02	0.19 ± 0.02	0.11 ± 0.02	132^{+8}_{-8}	35^{+3}_{-3}	STIS
HD 207198	0.21 ± 0.03	0.73 ± 0.05	0.88 ± 0.05	0.69 ± 0.05	0.52 ± 0.05	0.38 ± 0.04	0.21 ± 0.05	0.17 ± 0.04	0.13 ± 0.04	...	56^{+2}_{-1}	59^{+7}_{-5}	S07
HD 207308	0.35 ± 0.06	1.15 ± 0.13	1.48 ± 0.14	0.81 ± 0.13	0.50 ± 0.12	0.47 ± 0.11	0.41 ± 0.11	76^{+14}_{-10}	45^{+15}_{-12}	HSF
HD 207538	0.37 ± 0.11	1.58 ± 0.21	1.54 ± 0.11	1.32 ± 0.05	0.80 ± 0.05	0.72 ± 0.03	0.83 ± 0.07	0.45 ± 0.17	52^{+10}_{-8}	46^{+14}_{-13}	G06
HD 210121	0.36 ± 0.05	1.28 ± 0.08	1.34 ± 0.08	0.95 ± 0.08	0.68 ± 0.08	0.50 ± 0.07	0.18 ± 0.06	82^{+12}_{-6}	52^{+11}_{-9}	S07
HD 281159	0.21 ± 0.02	0.83 ± 0.03	0.75 ± 0.03	0.76 ± 0.03	0.48 ± 0.03	0.26 ± 0.03	0.24 ± 0.03	72^{+34}_{-10}	60^{+23}_{-17}	ARC

^aReferences: ARC = ARC echelle data; G99 = Gredel 1999; G06 = Galazutdinov et al. 2006; HIR = HIRES data; HSF = Hupe et al. 2012; IG11 = Iglesias-Groth 2011; K09 = Kaźmierczak et al. 2009; K10 = Kaźmierczak et al. 2010; S07 = Sonnentrucker et al. 2007; UV = UVES data; STIS = HST/STIS data; vDB = van Dishoeck & Black 1989; W20 = Welty et al. 2020

obtained with the NK20 collisional rate coefficients. Red: results obtained with the collisional cross-sections used by vDB82

One caveat here is that the excitation is modeled for a medium of constant temperature and density. There are indeed clear indications of multiple C_2 components, with somewhat different properties, for some sight lines (Sembach et al. 1996, CC12). If an admixture of widely-varying temperatures were present along the sightline, then the rotational diagram could acquire some degree of curvature, even in the high density limit where collisional excitation dominates radiative pumping. Widely-varying temperatures are not expected within diffuse molecular clouds that are heated by interstellar UV radiation, but might exist if shocks are present. More generally, the dissipation of turbulence can lead to additional heating terms that increase the temperature beyond that expected from UV photoelectric heating alone, but the fraction of the gas so affected is likely too small (e.g. Godard et al. 2009) to affect the C_2 rotational diagrams significantly.

A second caveat concerns the radiation field near $1\mu\text{m}$ that is primarily responsible for radiative pumping of C_2 . The density estimates we obtain are proportional to the radiative pumping rate that is assumed, W_J . The value adopted here is that expected given the mean ISRF assumed by vDB82, scaled by a factor 1.39 to match the $1.25\mu\text{m}$ measurements performed by *COBE*/DIRBE. Within diffuse molecular clouds, the radiation field might be reduced somewhat by attenuation by dust, although the effect is fairly minor at the relevant wavelengths, with the pumping rate decreasing with extinction along each ray, A_V , as $\exp(-0.35 A_V)$. Conversely, if the cloud is located close to a bright source of $1\mu\text{m}$ radiation, the radiation field could be enhanced. A more complete analysis, which we defer to a future paper, would involve computing the IR radiation at each point within an absorbing cloud, based upon the known three-dimensional distribution of nearby stars and dust. In the present study, we simply adopt the ISRF present at the solar neighborhood, as calibrated using the all-sky $1.25\mu\text{m}$ map obtained by DIRBE.

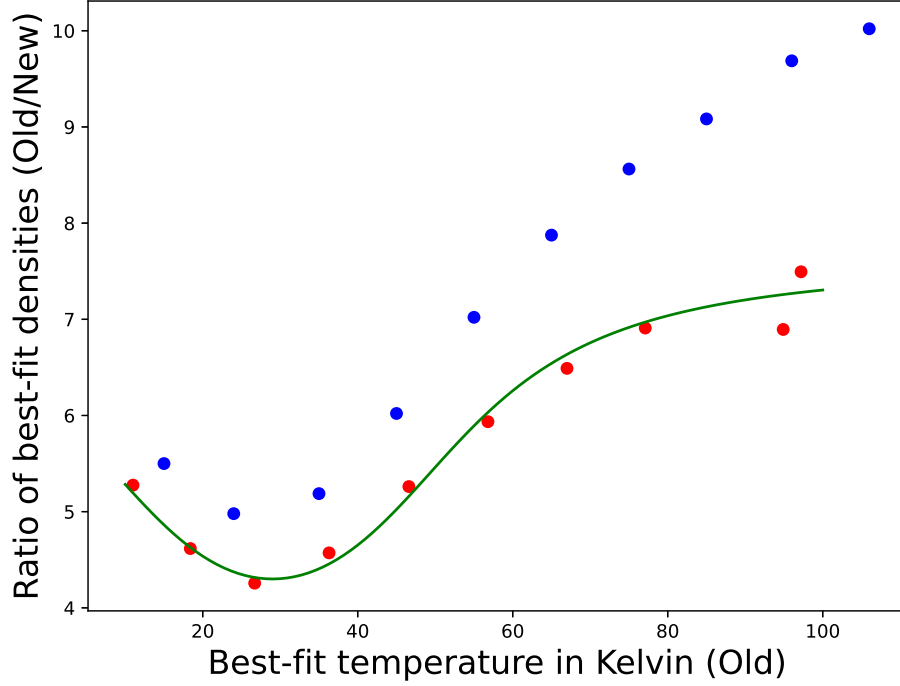


Figure 5. Ratio of the gas densities obtained with the vDB82 rate coefficients (blue points) to those obtained with the NK20 rate coefficients; the same IR radiation field and radiative excitation matrix are adopted in both cases. Red points show the ratio of the densities obtained with the OC to those obtained in the present work (i.e. with the NK20 rate coefficients). Results were obtained for rotational diagrams generated for $n_{\text{H}} = 80 \text{ cm}^{-3}$ with the collisional rates calculated by NK20. The green curve shows the fit to the red points presented in eqn. (2), and may be used to correct results obtained with the OC.

A third caveat is that we assume hydrogen to be entirely molecular within the region where C_2 is most abundant. This approximation is supported by the observational finding that the C_2 column densities measured toward background stars, $N(\text{C}_2)$, show a very strong dependence on the measured H_2 column densities, $N(\text{H}_2)$ (e.g. S07). This behavior is also consistent with chemical models (e.g. Federman & Huntress 1989) that suggest the formation of C_2 is initiated by reaction of C^+ and CH , the latter molecule being known to be a surrogate tracer for H_2 (Sheffer et al. 2008). In this context, it must be noted that the local atomic fraction, $n(\text{H})/[2n(\text{H}_2) + n(\text{H})]$, in the densest regions where C_2 is most abundant, is expected to be considerably smaller than the ratio of column densities for the entire sightline, $N(\text{H})/[2N(\text{H}_2) + N(\text{H})]$. Among the 24 sources in our sample for which H and H_2 measurements are available, the latter quantity has a median value of 0.56; by contrast, 3D PDR models (Obolentseva et al. 2024) for selected sources predict a local atomic fraction $\sim 0.02 - 0.06$ for the hydrogen in the densest material along the sightline (Obolentseva 2024, priv. comm.) In other words, the gas composition along any given sightline may be very variable, with the local H abundance, $n(\text{H})/n_{\text{H}}$, being reduced in the regions of highest density and anticorrelated with the C_2 abundance. Most of the H_2 and C_2 column

density along any diffuse cloud sightline is expected to come from the most highly shielded regions that surround the locations of maximum density. This behavior is invariably predicted by diffuse cloud models, dating back to the pioneering work of van Dishoeck & Black (1986), and is a consequence of the non-linear behavior caused by H_2 self-shielding. Because H_2 is photodissociated following line absorption in its ultraviolet Lyman and Werner bands, it is very effective in shielding itself once the line optical depths become significant (i.e. once $N(\text{H}_2) \gtrsim 10^{13} \text{ cm}^{-2}$), leading to a very strong dependence of the molecular fraction on the shielding column, N_{H} (e.g. Dishoeck & Black 1986; their Figure 3, which also shows a similarly strong dependence of the C_2 abundance). Subsequent analytic treatments (Sternberg et al. 2024, and references therein) indicate that for the densities of present interest, the H_2/H transition occurs at a shielding column density that is only logarithmically dependent on gas density. Thus, as shown by Obolentseva et al. (2024), H_2 self-shielding permits high molecular fractions to be achieved even at the lower gas densities inferred in our study.

Many cloud density estimates in the literature (e.g. Fan et al. 2023) have been obtained using an online calculator² (OC), developed by B. McCall, which fits any input set of level populations, f_J , and uses the collisional cross-sections adopted by vDB82. The results generated by this online calculator are slightly different from those that we obtain with the vDB82 collisional rates, because the OC uses an earlier treatment of radiative pumping (due to vDB82 rather than CC12) and a smaller assumed infrared radiation field. We used the following method to estimate the correction factor needed to correct density estimates obtained from the OC or from our own treatment with the vDB82 collisional rates, with results that are presented in Figure 5. We first used the NK20 rates to compute the rotational diagrams expected for fully molecular gas with a density $n_{\text{H}} = 80 \text{ cm}^{-3}$ and a gas temperature ranging from 10 to 100 K in steps of 10 K; and we then fit those rotational diagrams using the vDB82 rates. The best fit temperatures and densities are shown in Figure 5. Here, the red points show the values yielded by the OC, and the blue points show those obtained with our own treatment using the vDB82 rates. Both treatments recover the temperatures to within 6 K at any temperature, but the densities are overestimated by the factors indicated on the vertical axis.

Almost identical results are obtained if gas densities, n_{H} , of 40 cm^{-3} or 160 cm^{-3} are adopted in place of 80 cm^{-3} . For the OC, this factor is well fit by the expression

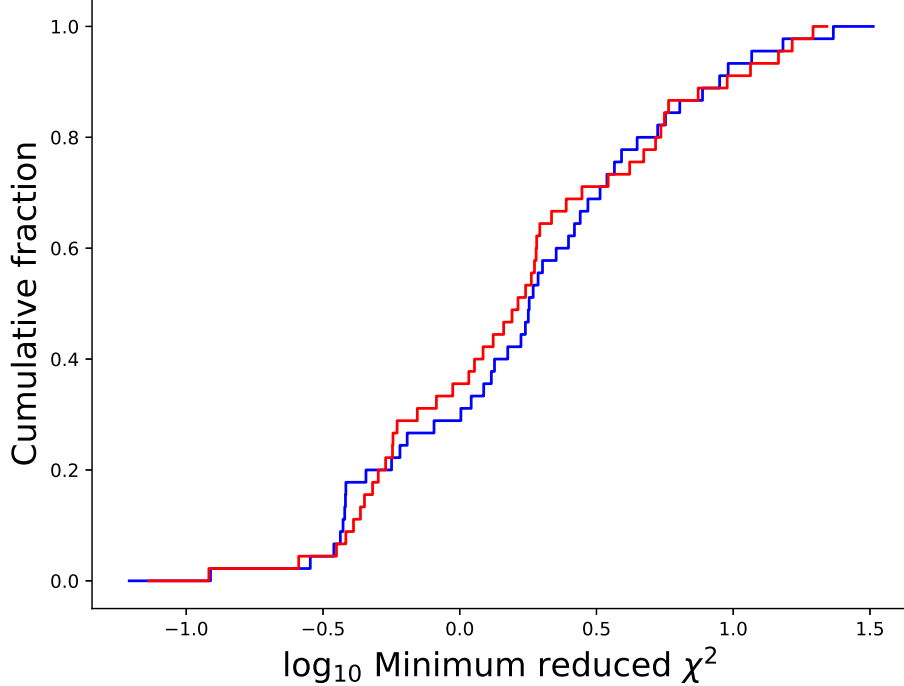
$$\frac{n(\text{OC})}{n(\text{NK20})} = 4.3 + 3.3 \frac{\tan^{-1}(0.0014 (T/\text{K} - 29)^2)}{\pi/2}, \quad (2)$$

(green curve) which may be used to obtain revised density estimates from literature estimates that were obtained with the OC. In cases where the fractional populations have also been published – which was not the case for Fan et al. (2023), however – a

² <http://dib.uiuc.edu/c2/>

revised calculator is available as a python script upon request to the corresponding author.

While the new rate coefficients reduce the best-fit densities by a factor 4 – 7 below the values obtained with the OC, the quality of the fits is indistinguishable. In other words, the fractional C_2 rotational populations, f_J , can be fit equally well for either set of adopted rate coefficients. Figure 6 shows the cumulative distribution functions for the minimum reduced χ^2 , with red and blue histograms applying to fits obtained with the vDB82 and NK20 rates, respectively. These distribution functions apply to the set of 46 rotational diagrams that we fit. In roughly 30% of cases, the minimum reduced- χ^2 was less than unity, implying that the stated error bars on the C_2 column densities were overestimates. For the remaining 70% of cases that yield a minimum reduced χ^2 greater than unity, either (1) the errors bars were underestimated; or (2) our simple constant-density constant-temperature excitation models fail to account fully for the observed rotational diagrams. In more than three-quarters of the 46 cases, the minimum reduced- χ^2 lies within the range 0.25 – 4. If the deviations from unity are the result of inaccuracies in the error bars (within an inhomogeneous set of reported observations), then the subset with minimum reduced χ^2 in the range 0.25 – 4 have error bars that are correct to within a factor 2.



[b]

Figure 6. Cumulative distribution functions for the minimum reduced χ^2 , with red and blue histograms applying to fits obtained with the vDB82 and NK20 rates, respectively

The gas temperature and density estimates obtained with the CC12 treatment of radiative excitation and the NK20 collisional rates are presented in Table 1, along with

the observed column densities, $N(J)$, in state J . In Figure 7, we present a compilation of the best-fit results and $1\text{-}\sigma$ error bars in the $n(\text{H}_2) - T$ plane. The black, magenta, blue, cyan, green and red curves show contours of constant gas pressure with $p/k = 1000, 1500, 2000, 2500, 3000$, and 3500 K cm^{-3} , respectively; here, we assume that the gas probed by C_2 is almost fully molecular and we include the contribution of He to the pressure. The mean and standard deviation of the best-fit $\log_{10}(p/k)$ estimates are 3.35 and 0.19, respectively – values that are in reasonable agreement with those obtained for the diffuse ISM by Jenkins & Tripp (2011) from observations of [CI] absorption (3.58 and 0.175) – although for individual sightlines where both [CI] and C_2 are observed, the pressure estimates may differ by up to a factor 20 in rare cases.

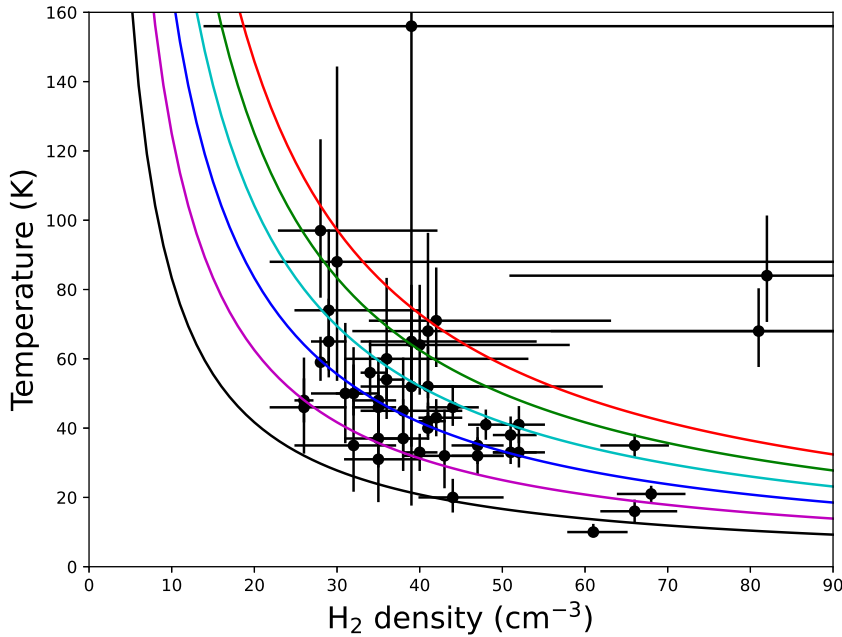


Figure 7. Best-fit results and $1\text{-}\sigma$ error bars in the $n(\text{H}_2) - T$ plane, for our sample of 46 background sources (Table 1). The black, magenta, blue, cyan, green and red curves show contours of constant gas pressure with $p/k = 1000, 1500, 2000, 2500, 3000$, and 3500 K cm^{-3} , respectively.

3. COMPARISON WITH DENSITIES DETERMINED FROM 3-DIMENSIONAL EXTINCTION MAPS

To perform a comparison with the C_2 -derived density estimates, we considered those 23 sources listed in Table 1 that have a *Gaia*-determined distance, d_{star} , within 1.25 kpc of the Sun (i.e. within the volume covered by the E23 extinction map). These are listed in Table 2. For each star, we computed the peak foreground density along the sightline implied by both the E23 and L20 extinction maps, as well as the heliocentric distances at which the density is maximal, $d_{\text{cloud}}(\text{E23})$ and $d_{\text{cloud}}(\text{L20})$. In cases where it is not entirely clear whether d_{cloud} is smaller or larger than d_{star} , we adopt a peak foreground density under the assumption that the star lies *behind* the cloud; in these cases, the adopted values may be overestimates.

In Figure 8, we show the density implied by the E23 extinction map within a plane of constant Galactic longitude, l , containing the line-of-sight to HD 24534. The vertical axis shows the distance in the Z -direction (perpendicular to the Galactic disk), and the horizontal axis shows the distance in the orthogonal direction within the slice of constant l . The Sun is located at the origin within each panel, and the dashed curve is the line-of-sight. The top left panel shows the entire region covered by E23, with the location of the background source marked with a cross. The other panels show successively zoomed regions centered on the Sun (top right) and the location along the sightline where the density is largest (bottom left). The E23 extinction maps cover heliocentric distances in the 69 – 1250 pc range, and the unmapped regions appear in white. As discussed in detail in E23, they are obtained from a Bayesian analysis of the available data. Twelve possible realizations of the extinction density – known as posterior estimates – are provided by E23, each of which may be regarded as equally probable. The densities plotted in Figure 8 are averages over these posterior estimates. Here, we adopted a column density conversion of $N_{\text{H}} = 5.3 \times 10^{21} \text{ cm}^{-2} E_{\text{ZGR}}$, where E_{ZGR} is the extinction defined by Zhang et al. (2023; hereafter ZGR), or equivalently $n_{\text{H}} = 1.7 \times 10^3 \text{ cm}^{-3} \times dE_{\text{ZGR}}/ds$ where s is the distance along the sightline in pc.

This conversion is based upon the universal extinction curve given by ZGR, which implies a V-band extinction, $A_V = 2.8 E_{\text{ZGR}}$; a ratio of A_V , to color excess, $E(B - V)$, of 3.1; and a ratio N_{H} to $E(B - V)$ of $5.8 \times 10^{21} \text{ cm}^{-2}$ (Bohlin et al. 1978). The latter two ratios imply that $N_{\text{H}}/A_V = 1.9 \times 10^{21} \text{ cm}^{-2}$. This value for N_{H}/A_V is in acceptable agreement with the mean value obtained subsequently by Rachford et al. (2009) for a sample of 17 sightlines: $(2.15 \pm 0.14) \times 10^{21} \text{ cm}^{-2}$. That sample (which is smaller than that presented by Bohlin et al. 1978) comprises the set of available non-Be stars with reliable $N(\text{H}_2)$ and $N(\text{H})$ obtained through ultraviolet observations. Variations about the best-fit N_{H}/A_V value for this sample (Rachford et al. 2009; see lower panel of their Figure 3) are barely larger than those expected from quoted measurement uncertainties. Assuming that the latter are correctly estimated, we find that the real rms sightline-to-sightline variation of N_{H}/A_V is only 12%. Naturally, any inaccuracies in the approximations discussed above would lead to inaccuracies in the inferred gas density, with the derived values of n_{H} being inversely proportional to the (G-band) extinction-to-gas ratio.

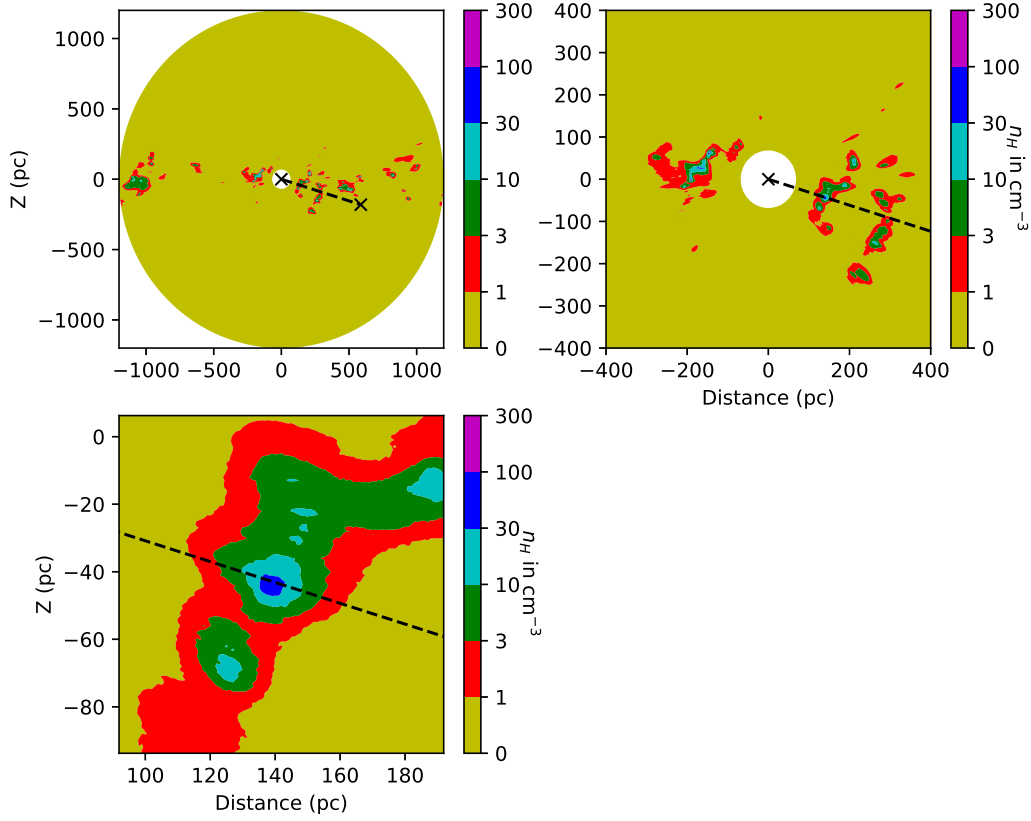


Figure 8. Gas density, n_{H} , implied by the E23 extinction map within a plane of constant Galactic longitude, l , containing the line-of-sight to HD 24534.

Figure 9 shows the density, n_{H} , averaged over the 12 posterior samples, as a function of distance along the sightline to HD 24534. The upper panel shows the density for the full sightline, using logarithmic spacing on vertical axis and with the location of the star indicated by the red cross. The lower panel zooms in on the region of maximum density, showing the mean density estimate in black and those from two individual samples in red and blue. These samples have the 2nd lowest and 2nd highest peak densities among the 12 posterior samples. We adopt the mean peak density within the 12 samples as our best estimate of the peak density along the sightline. As our lower and upper bounds, we adopt the peak values in the samples shown in red and blue. Two-thirds of the samples have peak density estimates lying between these two values and one-sixth of the samples have peak density estimates lying outside these two values (with the remaining one-sixth having peak density estimates equal to these two values). We may therefore regard these values as corresponding to 75% confidence limits, 75% being the mean of the fraction of peak density estimates lying inside the confidence limits (67%) and the fraction that are not outside the limits (83%). These peak density estimates are tabulated in Table 2.

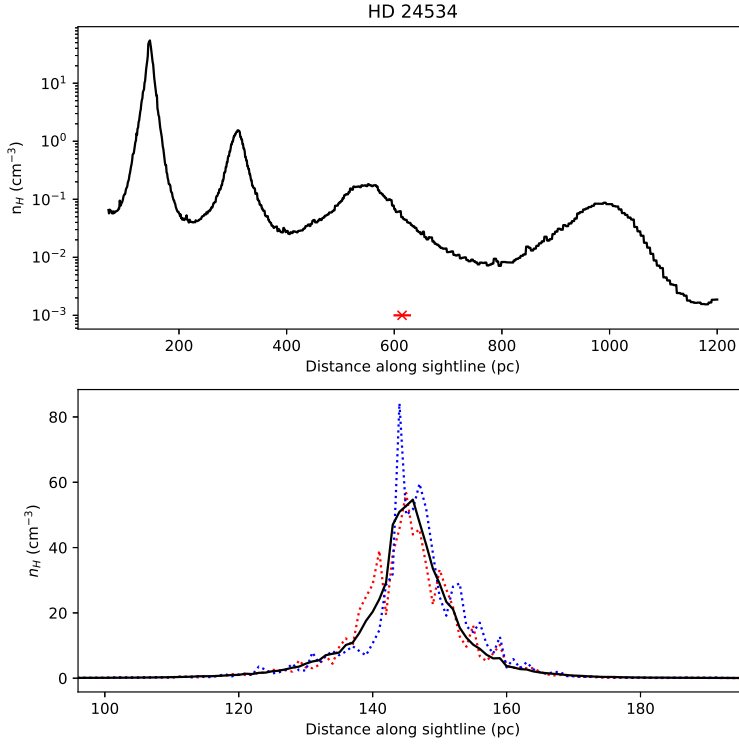


Figure 9. Gas density, n_{H} , averaged over the 12 posterior samples, as a function of distance along the sightline to HD 24534. Upper panel: $\log_{10}(n_{\text{H}}/\text{cm}^{-3})$ for the full sightline. Lower panel: $n_{\text{H}}/\text{cm}^{-3}$ near the region of maximum density, showing the mean density estimate in black and those from two individual samples in red and blue (see text).

In a similar manner, we obtained peak density estimates for the other 22 background sources lying within 1.25 kpc of the Sun. In Figure Set 1 (Appendix A), plots similar to Figure 1, Figure 4, and the bottom panels of Figures 8 and 9 are presented in a single figure for each source. An example is shown in Figure 10, where we present the results for a more distant cloud, located along the sightline to HD 204827.

Table 2. Cloud density and distance estimates

Source	l	b	n_{H} C ₂	n_{H} E23	n_{H}^a L20	d_{cloud} E23	d_{cloud}^a L20	d_{star} <i>Gaia</i> ^b
	(deg)	(deg)	(cm ⁻³)	(cm ⁻³)	(cm ⁻³)	(pc)	(pc)	(pc)
HD 24534	163.0814	-17.1362	70 ⁺⁴ ₋₆	71 ⁺¹³ ₋₁₄	101 ⁺⁴³ ₋₃₄	146	148	614 ⁺¹⁴ ₋₁₄
HD 27778	172.7629	-17.3928	64 ⁺² ₋₄	34 ⁺⁵ ₋₆	45 ⁺¹⁷ ₋₁₆	153	138	212 ⁺¹ ₋₁
HD 29647	174.0529	-13.3487	122 ⁺⁸ ₋₆	103 ⁺³⁴ ₋₃₁	263 ⁺⁹⁷ ₋₆₂	156	140	156 ⁺¹ ₋₁
HD 34078	172.0813	-2.2592	56 ⁺²⁸ ₋₁₀	9 ⁺¹ ₋₁	374	389 ⁺⁵ ₋₅
HD 62542	255.9153	-9.2371	104 ⁺⁶ ₋₄	13 ⁺³ ₋₃	313 ⁺⁷³ ₋₄₇	294	295	367 ⁺² ₋₂
HD 73882	260.1816	0.6431	132 ⁺¹⁰ ₋₈	17 ⁺⁶ ₋₄	899	461 ⁺³³³ ₋₁₃₆
HD 147084	352.3279	18.0503	62 ⁺⁸ ₋₈	244 ⁺³⁴ ₋₃₆	172 ⁺⁷⁴ ₋₅₈	150	132	270 ⁺⁴⁶ ₋₃₄
HD 147888	353.6470	17.7092	68 ⁺⁴ ₋₂	230 ⁺³⁹ ₋₄₁	189 ⁺⁷⁴ ₋₆₉	150	133	124 ⁺⁶ ₋₆
HD 147889	352.8573	17.0436	72 ⁺⁴ ₋₂	189 ⁺²⁵ ₋₁₉	149 ⁺¹²⁴ ₋₅₄	150	132	136 ⁺⁰ ₋₀
HD 147933	353.6860	17.6867	84 ⁺⁶ ₋₄	225 ⁺⁴⁰ ₋₃₉	184 ⁺⁷² ₋₆₈	150	136	138 ⁺³ ₋₂
HD 148184	357.9328	20.6766	78 ⁺³⁰ ₋₁₂	73 ⁺¹¹ ₋₁₁	53 ⁺²² ₋₂₃	150	117	153 ⁺⁵ ₋₄
HD 149757	6.2812	23.5877	52 ⁺² ₋₂	45 ⁺¹² ₋₉	42 ⁺²⁰ ₋₁₄	107	105	112 ⁺³ ₋₂
HD 154368	349.9702	3.2151	80 ⁺⁴ ₋₄	93 ⁺¹⁶ ₋₁₉	75 ⁺²⁸ ₋₂₃	201	200	1064 ⁺⁴⁰ ₋₃₇
HD 170740	21.0574	-0.5259	70 ⁺¹⁰ ₋₈	50 ⁺¹⁶ ₋₁₂	35 ⁺¹⁵ ₋₁₇	228	226	226 ⁺⁵ ₋₄
HD 179406	28.2285	-8.3118	162 ⁺³²⁶ ₋₅₀	19 ⁺⁴ ₋₄	43 ⁺⁴⁶ ₋₂₄	227	225	289 ⁺¹⁰ ₋₉
HD 203532	309.4590	-31.7397	70 ⁺⁸ ₋₈	43 ⁺¹² ₋₁₁	92 ⁺⁶¹ ₋₄₂	205	206	291 ⁺² ₋₂
HD 204827	99.1667	5.5525	102 ⁺⁶ ₋₄	14 ⁺³ ₋₃	461	929 ⁺⁹⁴ ₋₇₈
HD 206267	99.2904	3.7383	132 ⁺⁸ ₋₈	7 ⁺¹ ₋₁	461	735 ⁺¹⁴¹ ₋₁₀₂
HD 207198	103.1363	6.9949	56 ⁺² ₋₁	11 ⁺² ₋₂	426	1002 ⁺³⁵ ₋₃₃
HD 207308	103.1090	6.8176	76 ⁺¹⁴ ₋₁₀	8 ⁺¹ ₋₂	426	924 ⁺¹⁴ ₋₁₄
HD 207538	101.5990	4.6727	52 ⁺¹⁰ ₋₈	17 ⁺⁴ ₋₅	458	849 ⁺¹² ₋₁₂
HD 210121	56.8751	-44.4610	82 ⁺¹² ₋₆	37 ⁺¹² ₋₁₃	29 ⁺⁸ ₋₉	239	240	334 ⁺⁴ ₋₄
HD 281159	160.4908	-17.8022	72 ⁺³⁴ ₋₁₀	95 ⁺²⁸ ₋₂₀	115 ⁺⁵⁰ ₋₃₀	307	302	152 ⁺²⁵⁰ ₋₅₈

^a Where $d_{\text{cloud}}(\text{E23})$ lies outside the volume covered by the L20 maps, no entry is given.

^b Gaia Collaboration (2020)

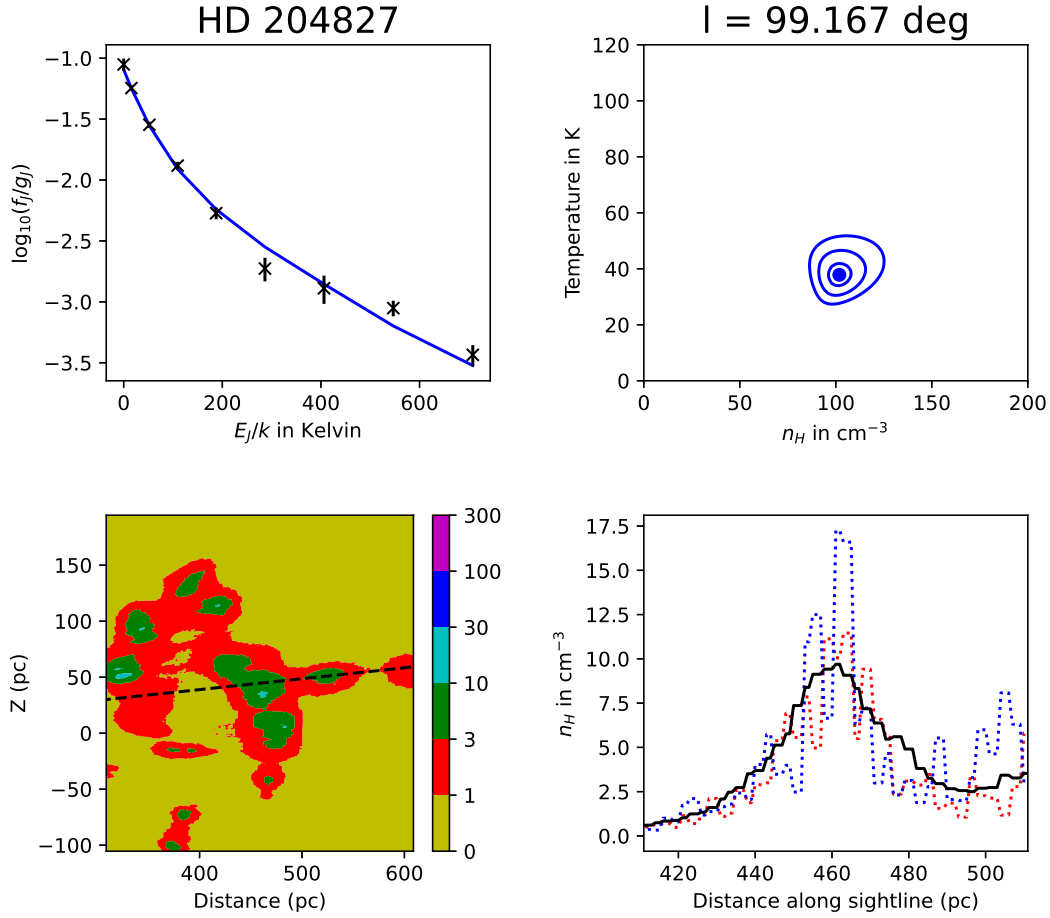


Figure 10. Summary of results for the sightline to HD 204827. The complete figure set (23 images, one for each sightline) is available in the online journal. Top left: Rotational diagram from C_2 absorption line observations. Top right: Contours of constant χ^2 in the plane of gas density, n_H , and kinetic temperature, T , for the fit to the C_2 rotational diagram; here we show 1σ , 2σ , and 3σ error ellipses obtained with the NK20 collisional rate coefficients. Bottom left: Gas density, n_H , implied by the E23 extinction map within a plane of constant Galactic longitude, l , containing the line-of-sight to the source. Bottom right: gas density, n_H , averaged over the 12 posterior samples from E23, as a function of distance along the sightline (black). Results from two individual samples are shown in red and blue (see text).

For the 17 sources where the position of peak density lies within the (smaller) volume covered in the L20 map, we used entirely analogous methods to compute the peak density given by the L20 map. The comparison between the peak line-of-sight density estimates in the two maps is shown in the top left panel of Figure 11. Most of the estimates agree within the 75% confidence limits obtained using the method described above. These errors, however, are statistical in nature and do not capture systematic uncertainties in the model (see E23’s Section 6).

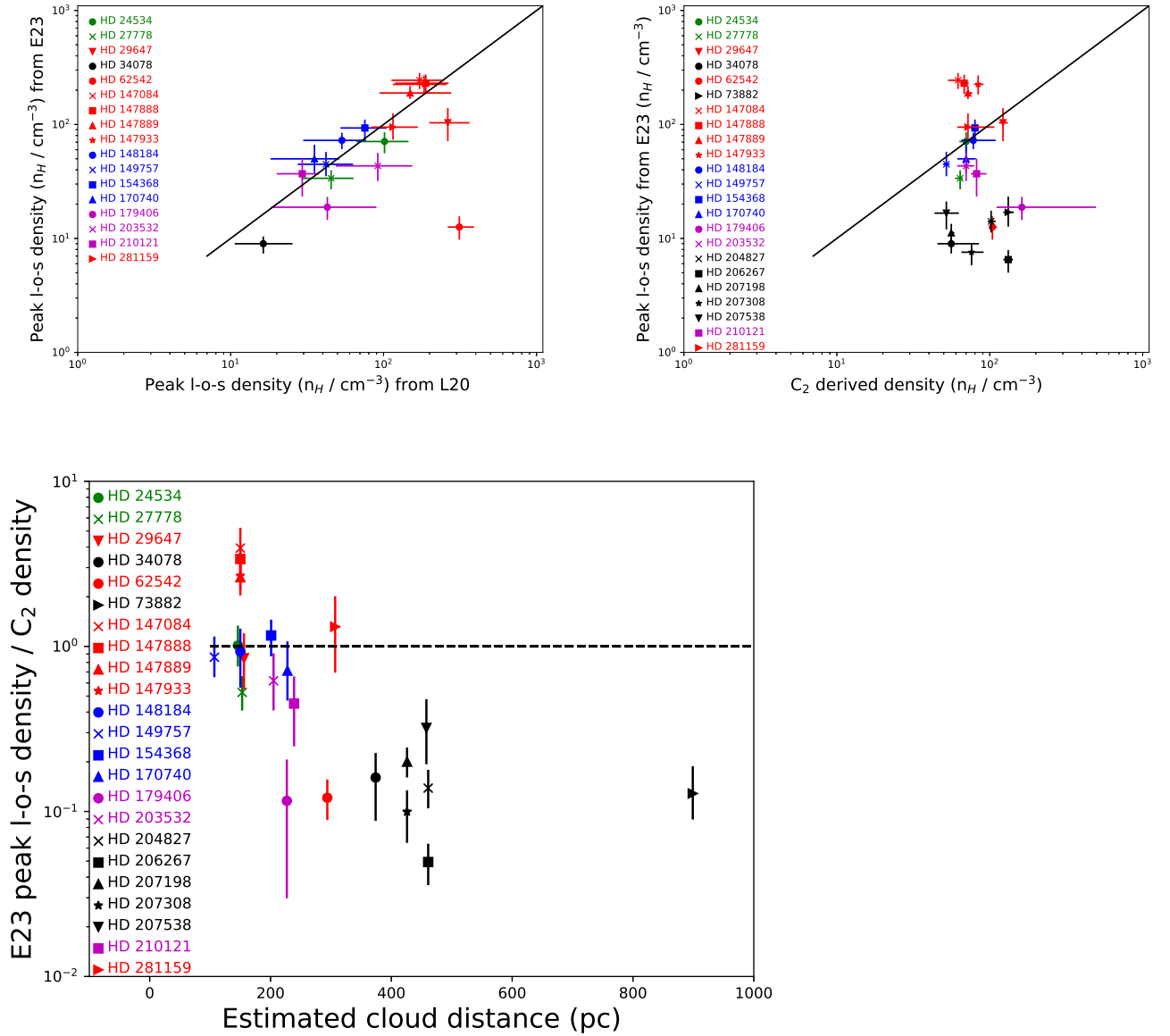


Figure 11. Top left: comparison between the peak line-of-sight density estimates in the L20 and E23 extinction maps, for 17 sources. Top right: comparison between the peak densities obtained from the E23 maps with the densities derived from C_2 . Bottom: ratio of E23 extinction map density estimate to C_2 density estimate as a function of the estimated cloud distance.

The red circle, applying to the sightline toward HD 62542, is an outlier; this is a rare region where the resolution in the plane-of-the sky is insufficient to yield reliable density estimates for the small dust cloud that HD 62542 is likely associated with. A dearth of background stars in the vicinity of $l \sim 352^\circ$, $b \sim 18^\circ$ makes the extinction maps unreliable for four additional sightlines (to HD 147084, HD 147888, HD 147889, and HD 147933). Similarly, HD 29647 and HD 281159 lie behind regions where the density of stars is insufficient to yield reliable results. These six cases are also plotted with red symbols in Figure 11.

In the top right of Figure 11, we compare the peak densities obtained from the E23 maps with the densities derived from C_2 . C_2 is expected to probe the densest material along the sightline because it is formed via a reaction sequence initiated by the reaction of C^+ with CH (Federman and Huntress 1989) and CH is most abundant where the gas is denser and more molecular. The black line at 45 degrees indicates where the two density estimates are equal. At least in an average sense, the new NK20 collisional rates bring the C_2 density estimates into reasonable agreement with the peak densities inferred from the E23 extinction maps: the median best-fit values for the two estimates are $n_H = 72 \text{ cm}^{-3}$ and 44 cm^{-3} , respectively, and mean best-fit values are $n_H = 81 \text{ cm}^{-3}$ and 74 cm^{-3} .

The four points (red symbols) lying significantly above the black line are precisely those in the vicinity of $l \sim 352^\circ$, $b \sim 18^\circ$, where a dearth of background stars makes the extinction maps unreliable.

Of the eight points lying significantly below the line, one applies to the sightline HD 62542 (red circle) where the extinction map estimate is also known to be unreliable. Six of the remaining seven points represent the most distant density peaks in the sample (all lying more than 350 pc from the Sun – see Table 2). These cases are represented by black symbols. Since the spatial resolution of the extinction maps worsens with increasing heliocentric distance, we speculate that these may be cases where the density peak is smeared out by inadequate resolution along the sightline. This speculation is supported by the map shown in Figure 10 (bottom left panel), in which the gas exhibits artificial extensions (“fingers of God”) pointing towards the Sun. The bottom panel of Figure 11 shows the ratio of extinction map density estimate to C_2 density estimate as a function of the estimated cloud distance.

For the 11 sightlines with (1) sufficient background stars to yield reliable extinction map density estimates and (2) where the density peak lies within 350 pc of the Sun, the best-fit C_2 density estimates agree within a factor 2 in all but one case. For this subset of the sightlines, we computed the mean density with a weighting inversely proportional to the squares of the uncertainties. The values obtained from the extinction maps and from the C_2 observations are $n_H = 56 \text{ cm}^{-3}$ and 65 cm^{-3} respectively, values that agree to within a factor better than 1.2.

4. DISCUSSION

Our significant downwards revision in the cloud density estimates derived from observations of C_2 – which is corroborated by the extinction maps as discussed in Section 3 – has implications for our understanding of the diffuse ISM. In particular, C_2 density estimates have been widely used in deriving the cosmic-ray ionization rate (CRIR) from absorption line observations of the H_3^+ molecular ion (McCall et al. 2003, Indriolo et al. 2007, Indriolo & McCall 2012). Density estimates are essential for this purpose because the H_3^+ molecular ion is formed at a rate per H_2 molecule that is dependent on the CRIR and destroyed at a rate that is proportional to the gas

density. The abundance of H_3^+ relative to H_2 is therefore dependent on the ratio of the CRIR to the gas density. The derived CRIR, in turn, depends on what is assumed for the gas density and will accordingly be reduced significantly. In our earlier study of the CRIR (Neufeld and Wolfire 2017; hereafter NW17), we obtained an average estimate of the primary ionization rate per H atom, $\zeta_p(\text{H})$, of $(2.3 \pm 0.6) \times 10^{-16} \text{ s}^{-1}$. The error given here is simply the standard error on the mean, without inclusion of possible systematic effects, and the value is the mean obtained for 7 “gold-plated” sightlines for which direct absorption line observations were available for H_2 , C_2 and H_3^+ (at ultraviolet, near-infrared and mid-infrared wavelengths respectively). The C_2 density estimates adopted were literature values that had been obtained with the online calculator.

Of the 7 sightlines with absorption line observations for H_2 , C_2 , and H_3^+ , four have C_2 observations covering $J \geq 12$ and are therefore in the sample adopted in the present work (HD 24534, HD 27778, HD 73882, and HD 154368). Using the revised NK20 rate coefficients to obtain density estimates for these sightlines, we used the diffuse cloud models of NW17 to obtain estimates of the CRIR from the observed H_3^+ abundances: the mean value was $\zeta_p(\text{H}) = 8 \times 10^{-17} \text{ s}^{-1}$, corresponding to a total ionization rate per H_2 molecule of $\zeta_t(\text{H}_2) = 1.8 \times 10^{-16} \text{ s}^{-1}$. The actual CRIR may be even lower, because C_2 is likely weighted toward denser, more fully-molecular gas than H_3^+ .

With the availability of the 3D density maps derived from E23 and L20 – and validated to some extent in Section 3 above – it is now possible to construct more sophisticated models than the simple constant density slab models adopted by NW17. In a companion paper by Obolentseva et al. (2024), such models are used to obtain predictions of the H_3^+ density in 3 dimensions, as a function of the CRIR. These can then be compared with the H_3^+ column densities observed along each sightline, thereby providing estimates of the CRIR and how it varies.

We are very grateful to F. Najar for providing full results from NK20 in machine-readable tables.

APPENDIX

Figure Set 1
(see Figure 10 for full caption)

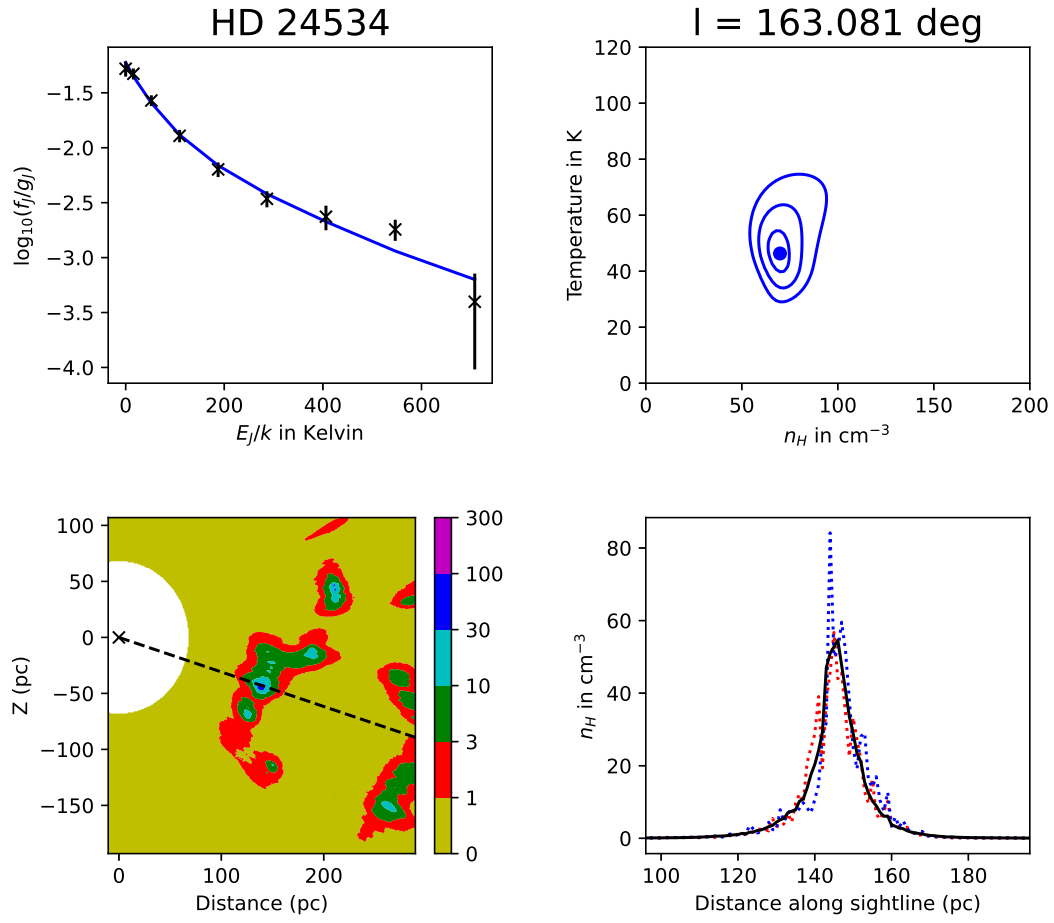


Figure 10.1. Results for the line-of-sight to HD 24534

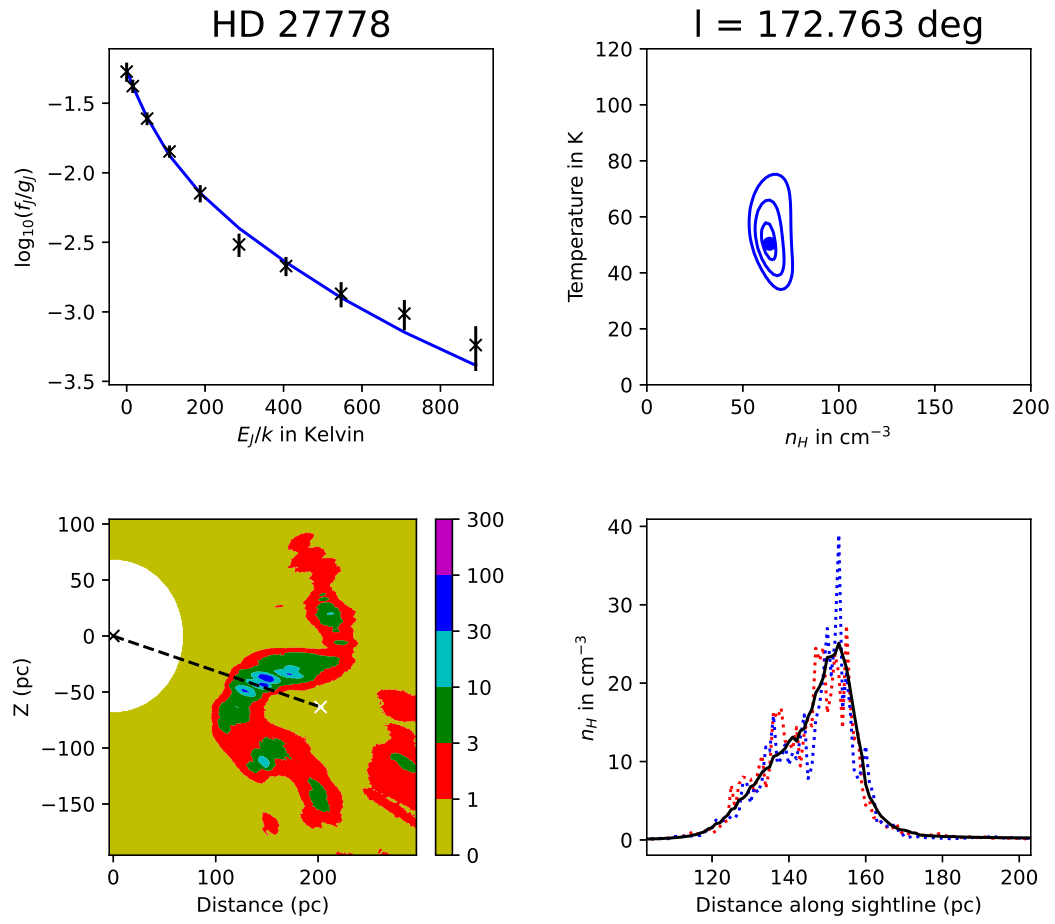


Figure 10.2. Results for the line-of-sight to HD 27778

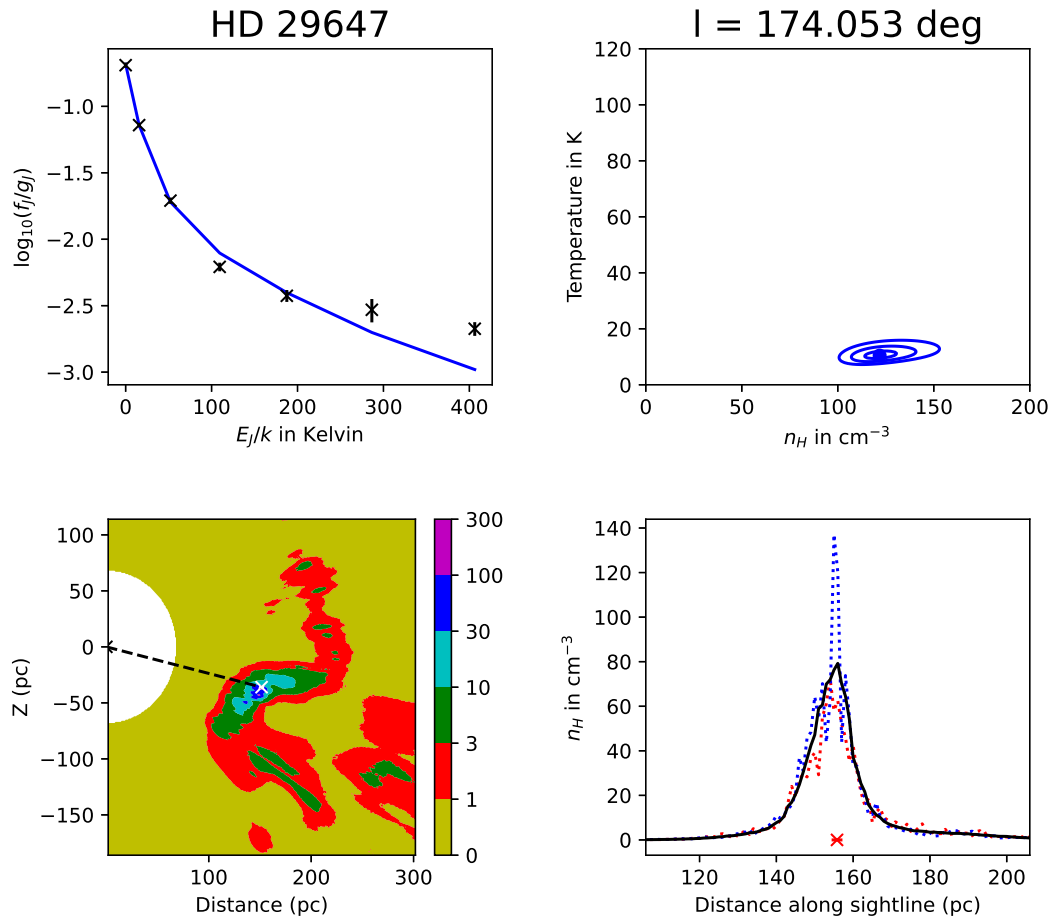


Figure 10.3. Results for the line-of-sight to HD 29647

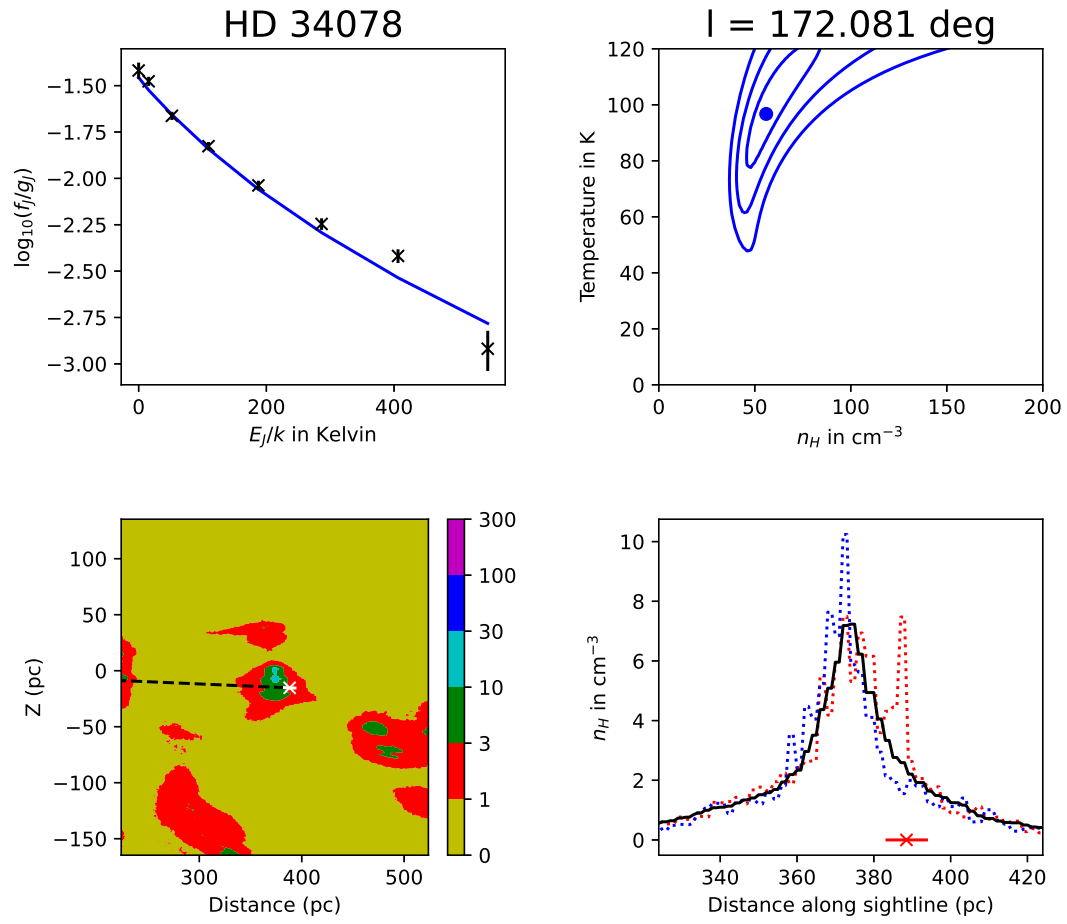


Figure 10.4. Results for the line-of-sight to HD 34078

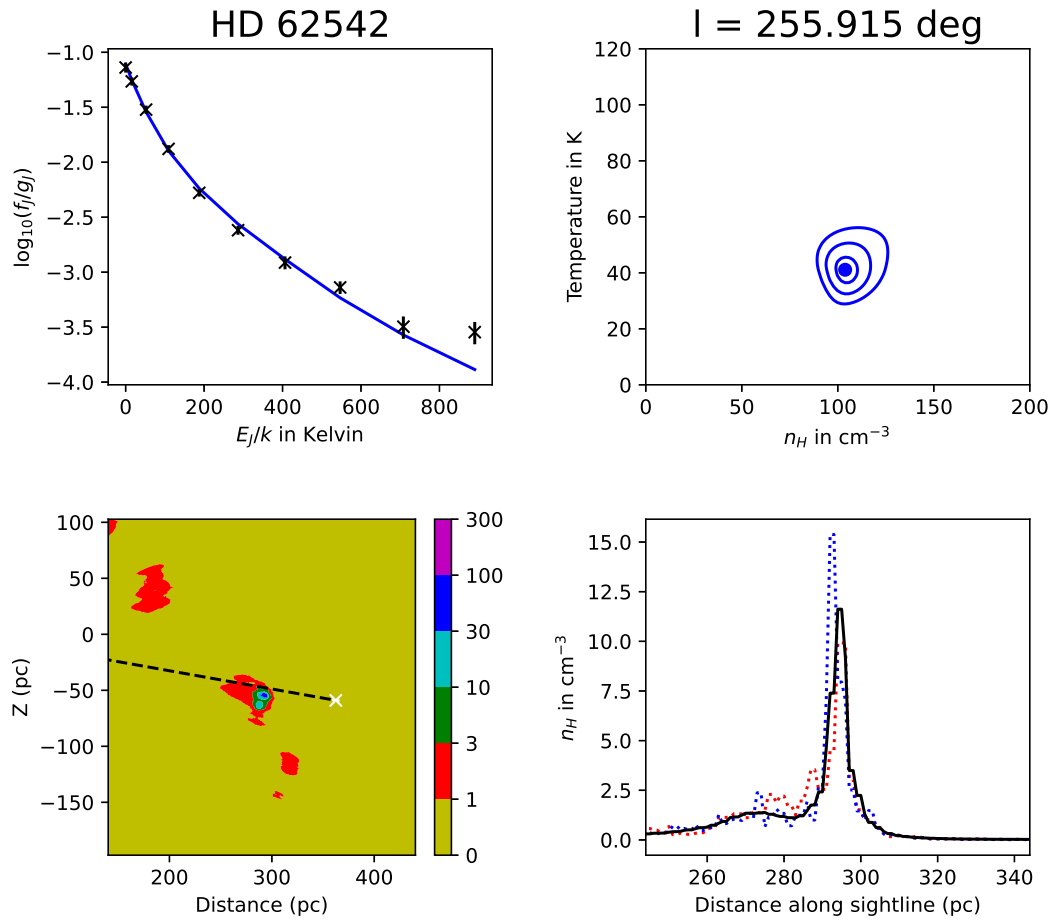


Figure 10.5. Results for the line-of-sight to HD 62542

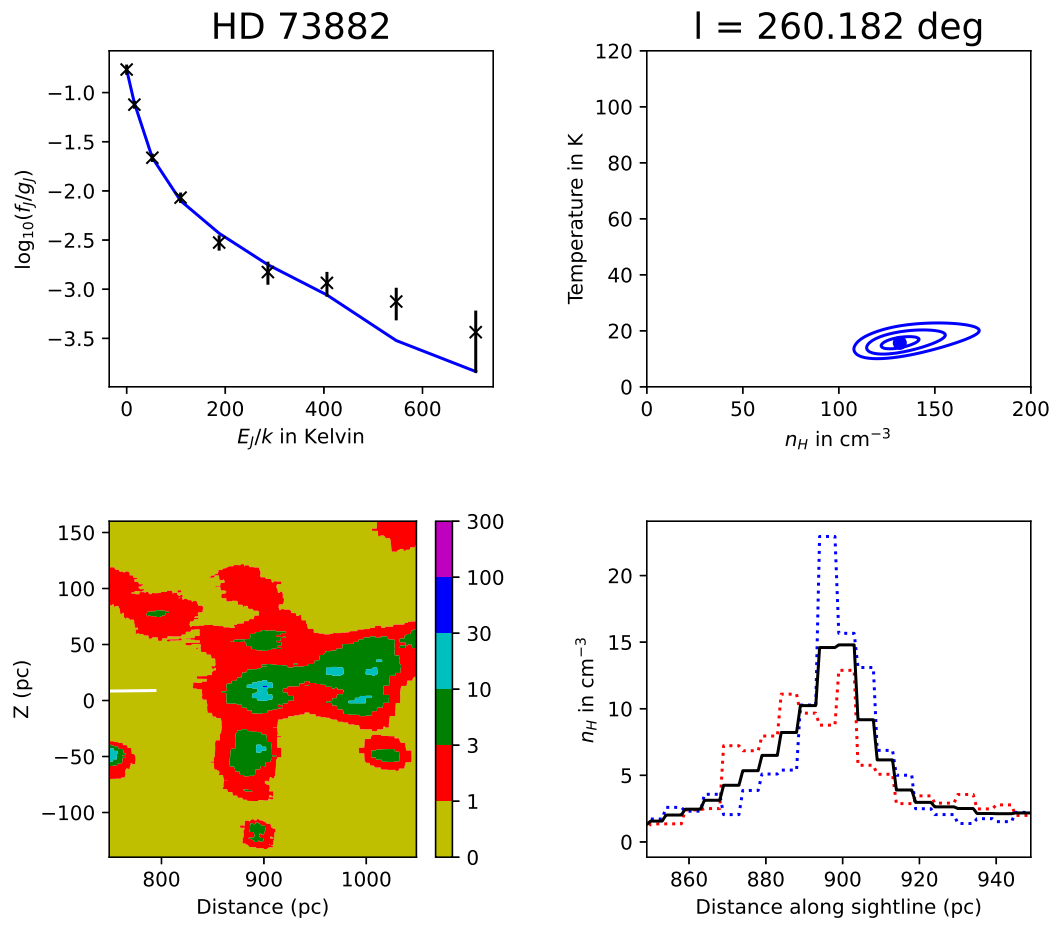


Figure 10.6. Results for the line-of-sight to HD 73882

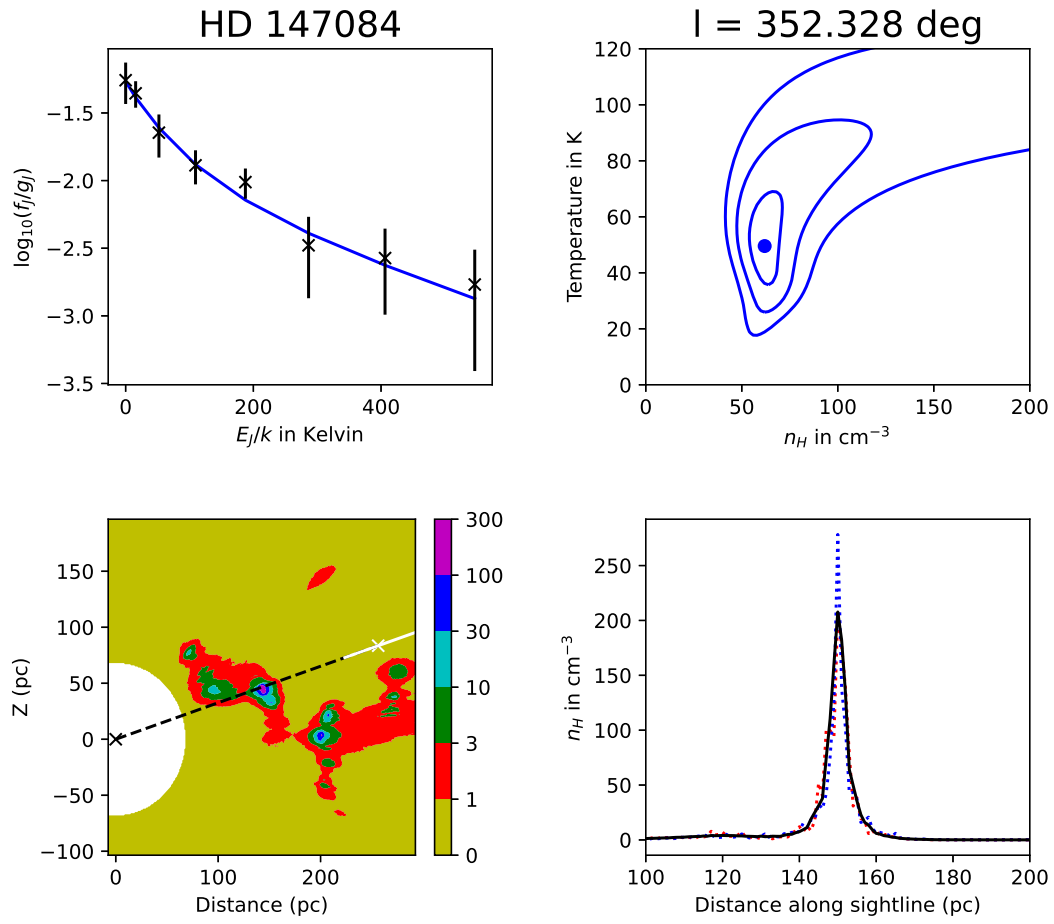


Figure 10.7. Results for the line-of-sight to HD 147084

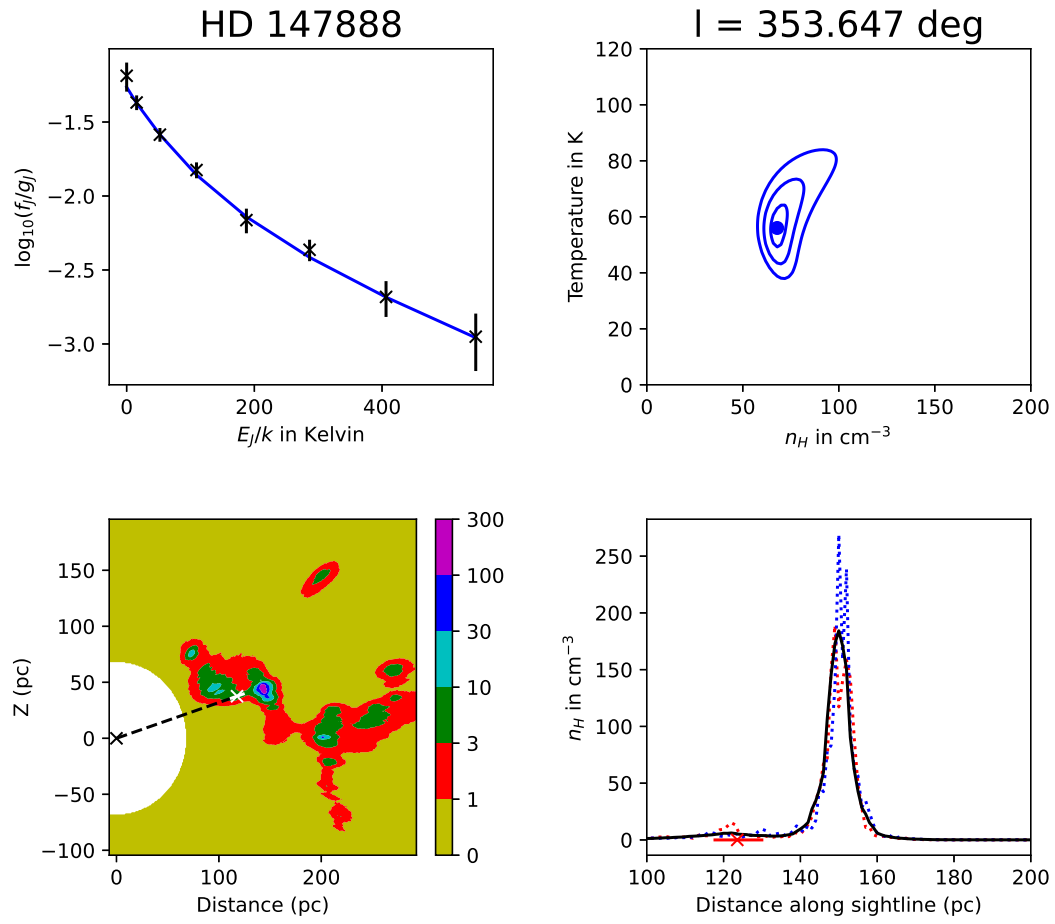


Figure 10.8. Results for the line-of-sight to HD 147888

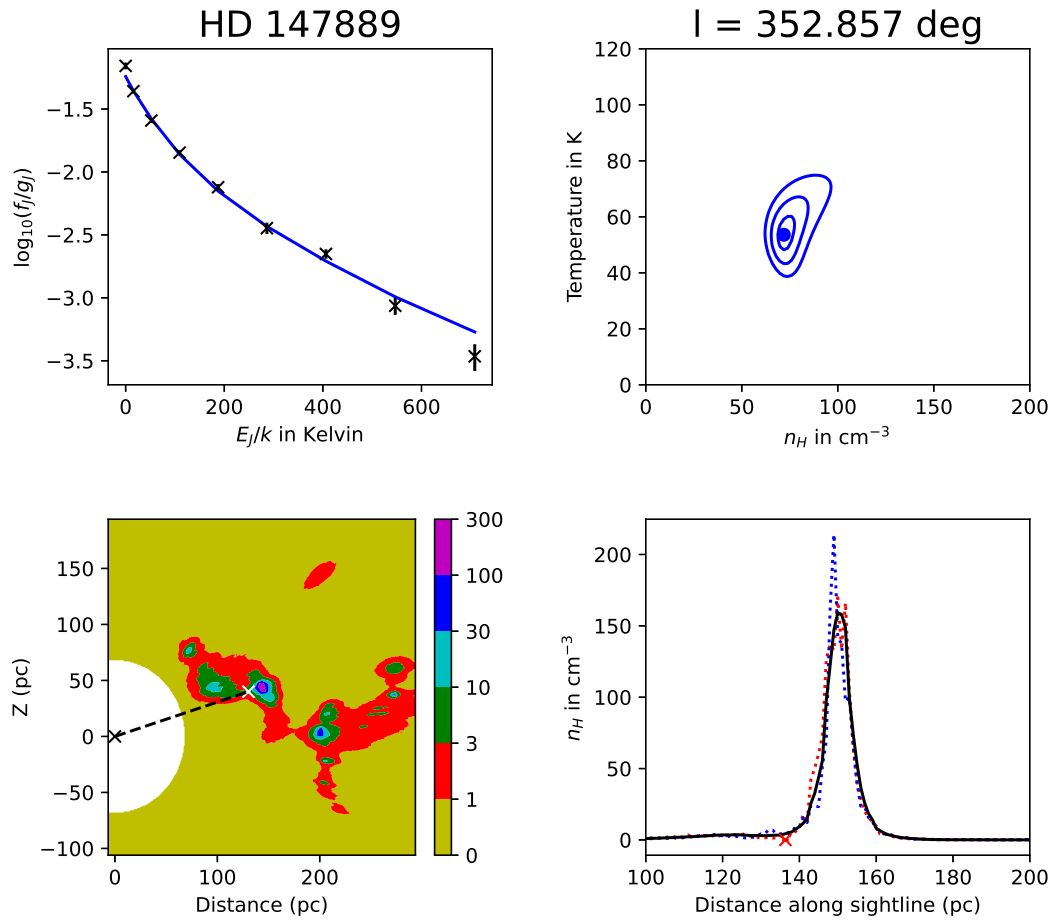


Figure 10.9. Results for the line-of-sight to HD 147889

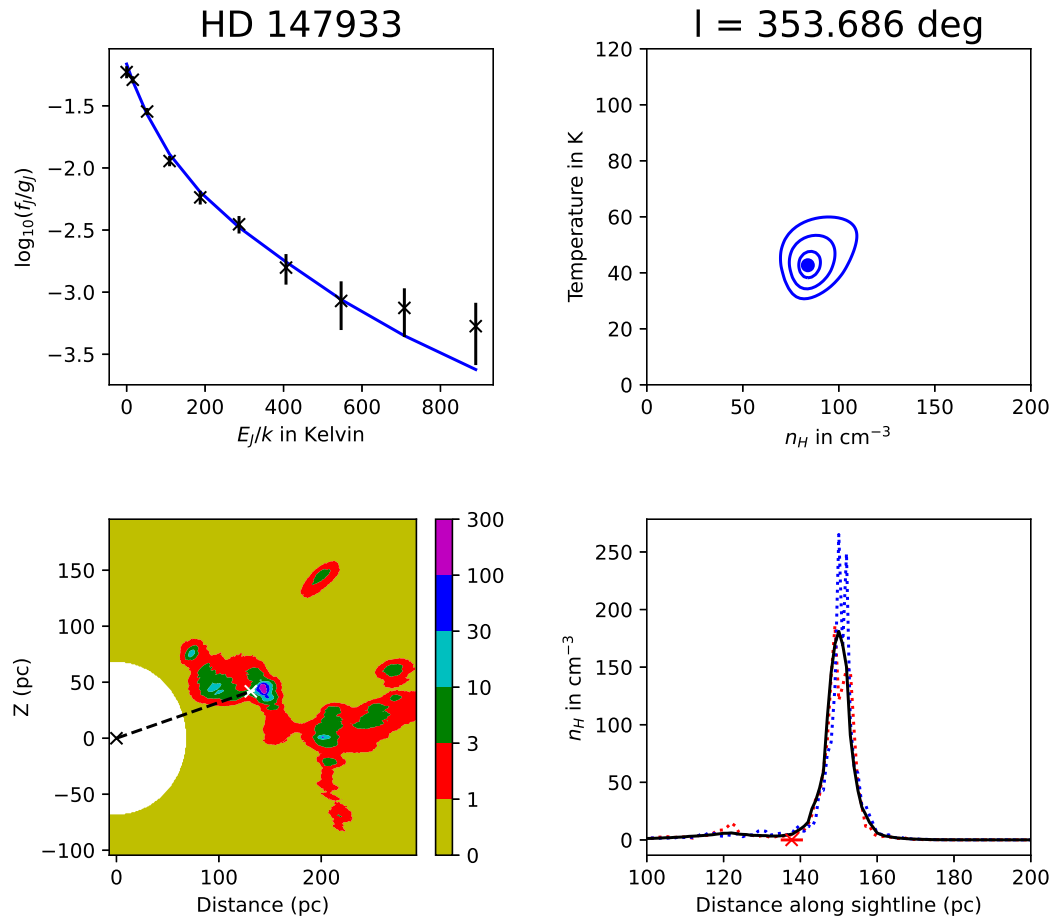


Figure 10.10. Results for the line-of-sight to HD 147933

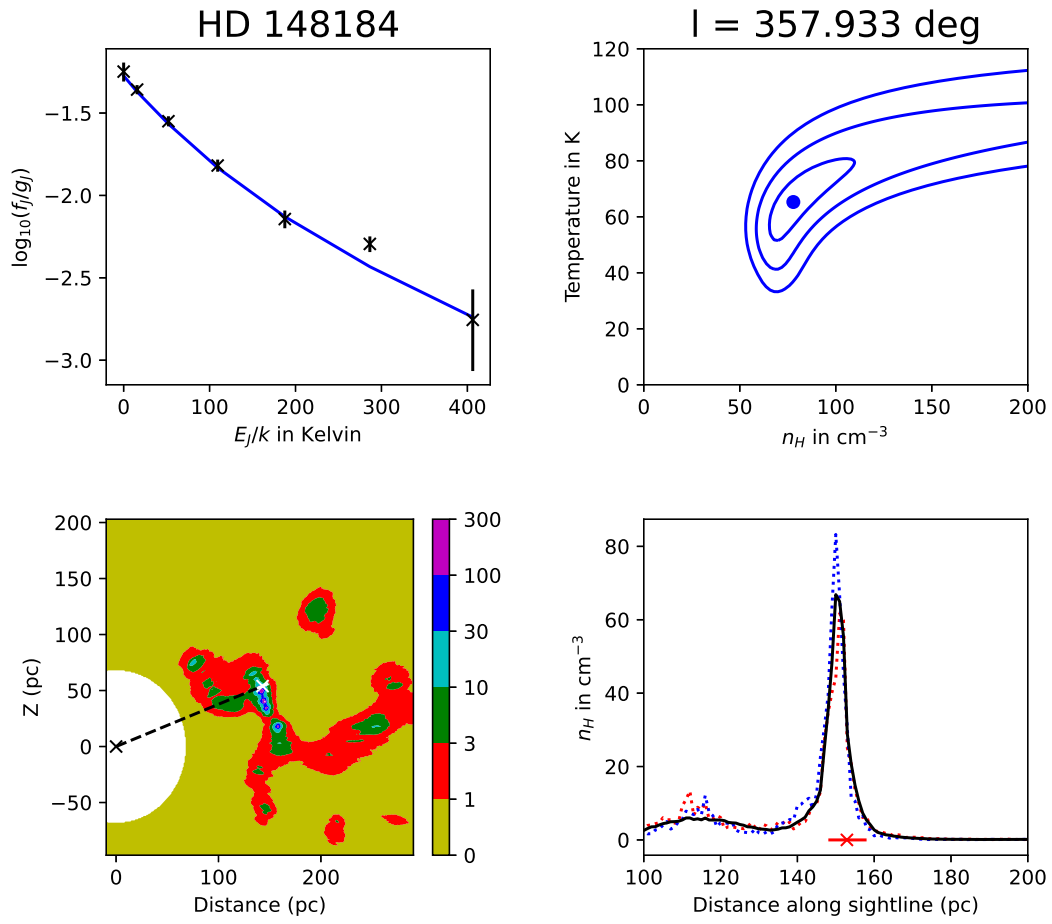


Figure 10.11. Results for the line-of-sight to HD 148184

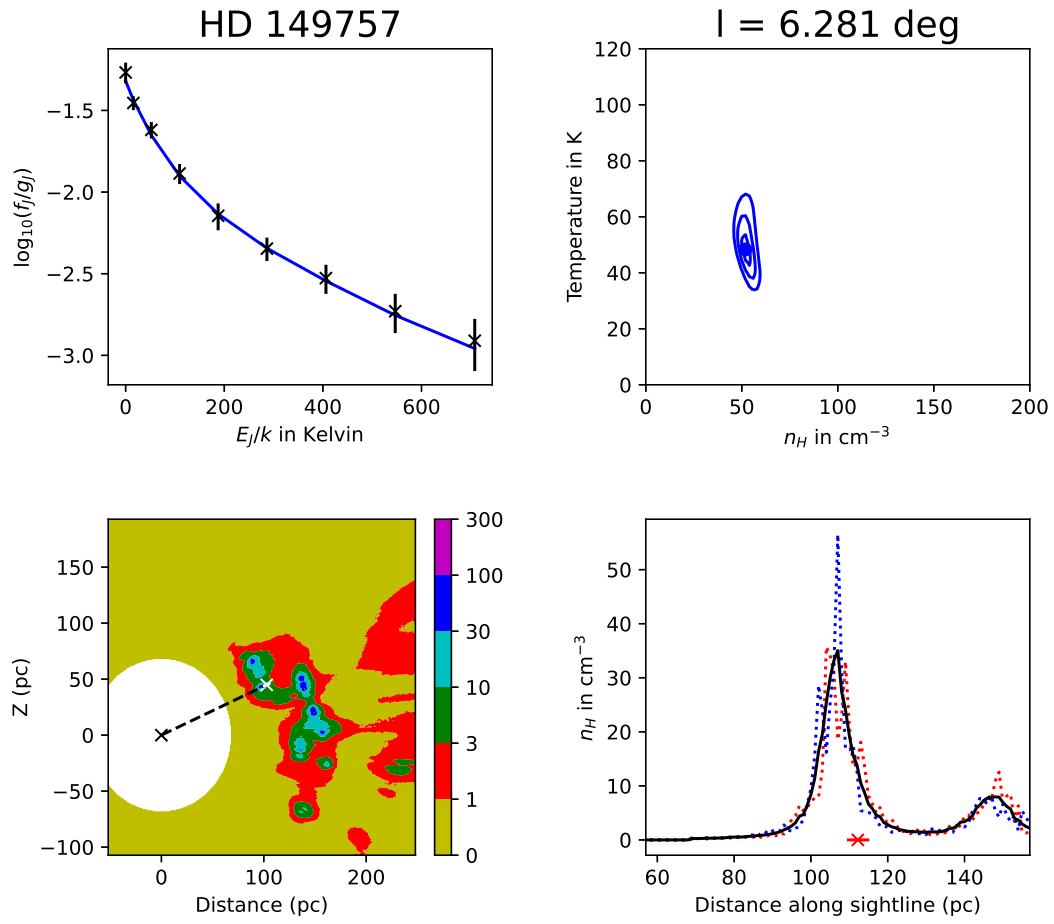


Figure 10.12. Results for the line-of-sight to HD 149757

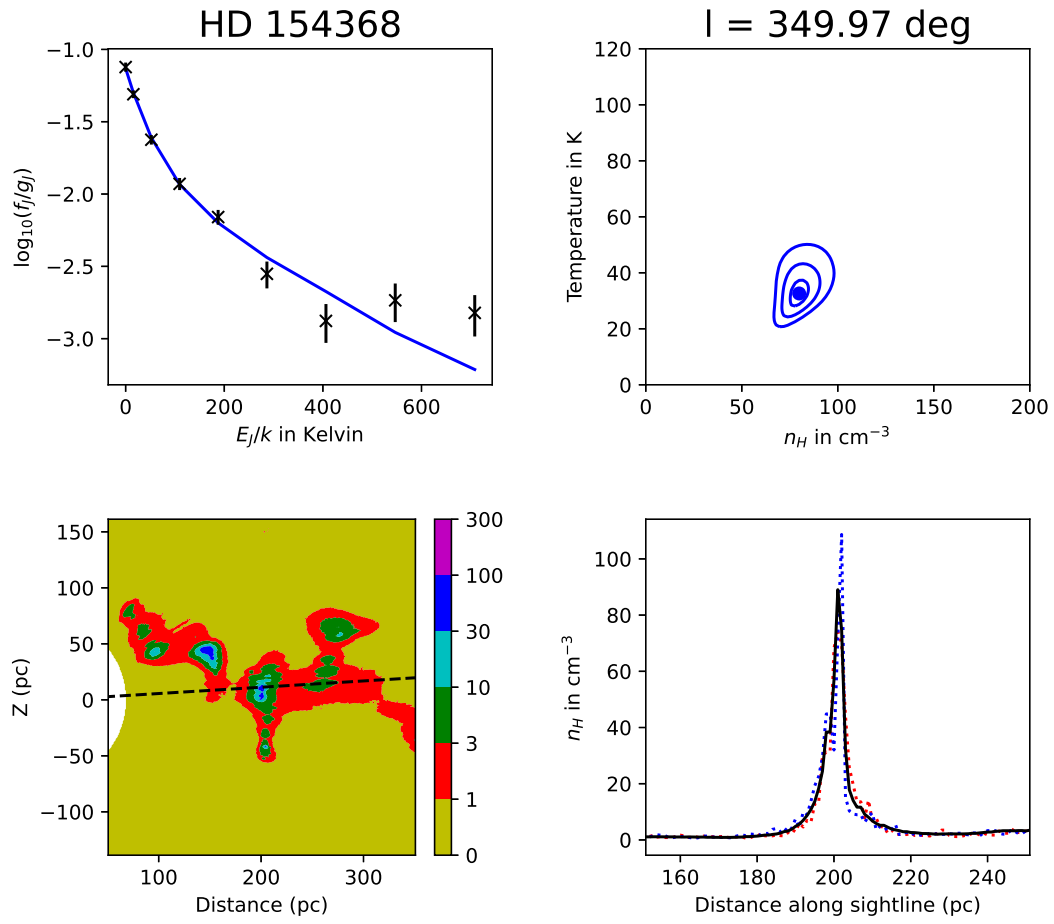


Figure 10.13. Results for the line-of-sight to HD 154368

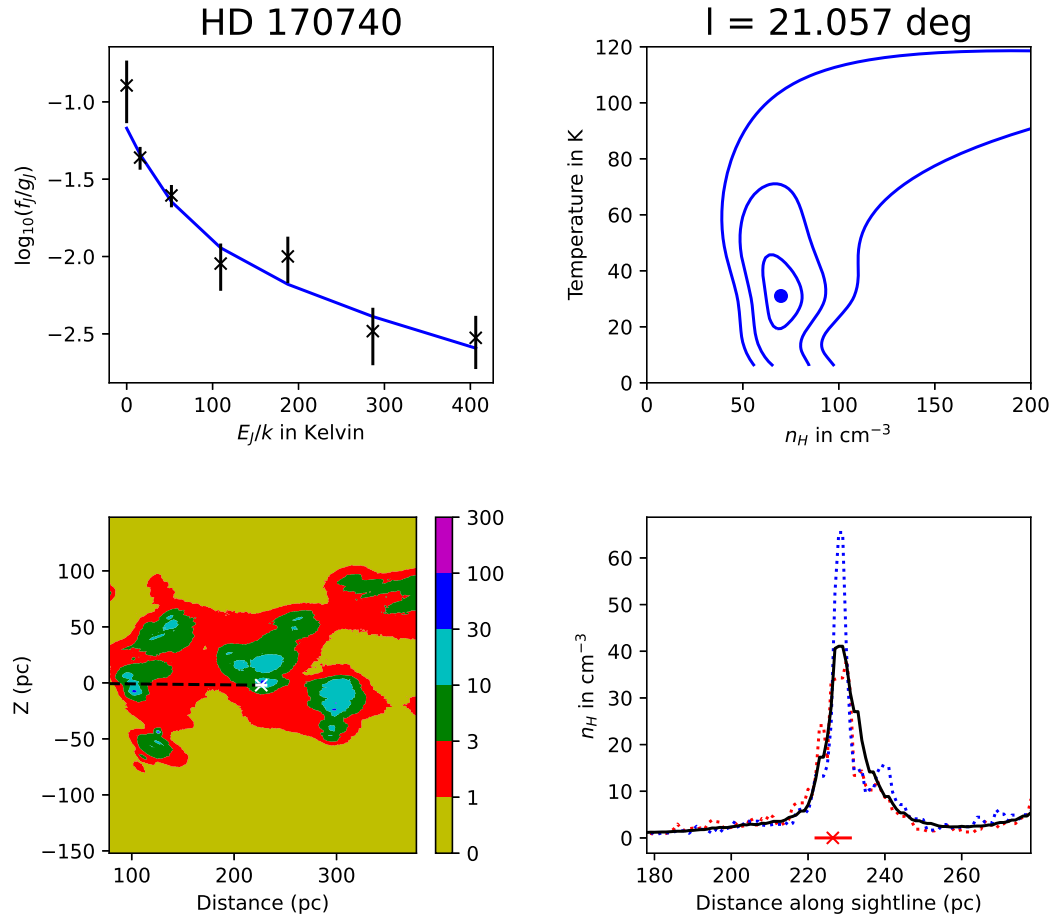


Figure 10.14. Results for the line-of-sight to HD 170740

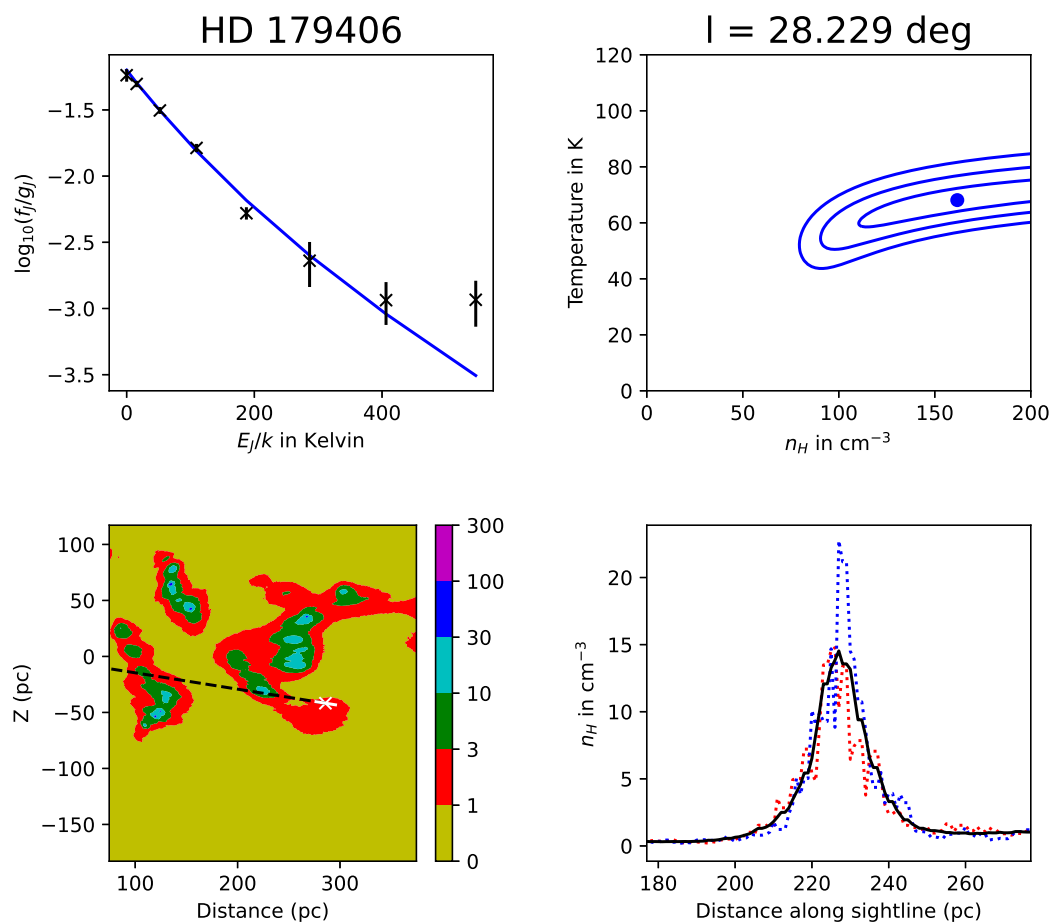


Figure 10.15. Results for the line-of-sight to HD 179406

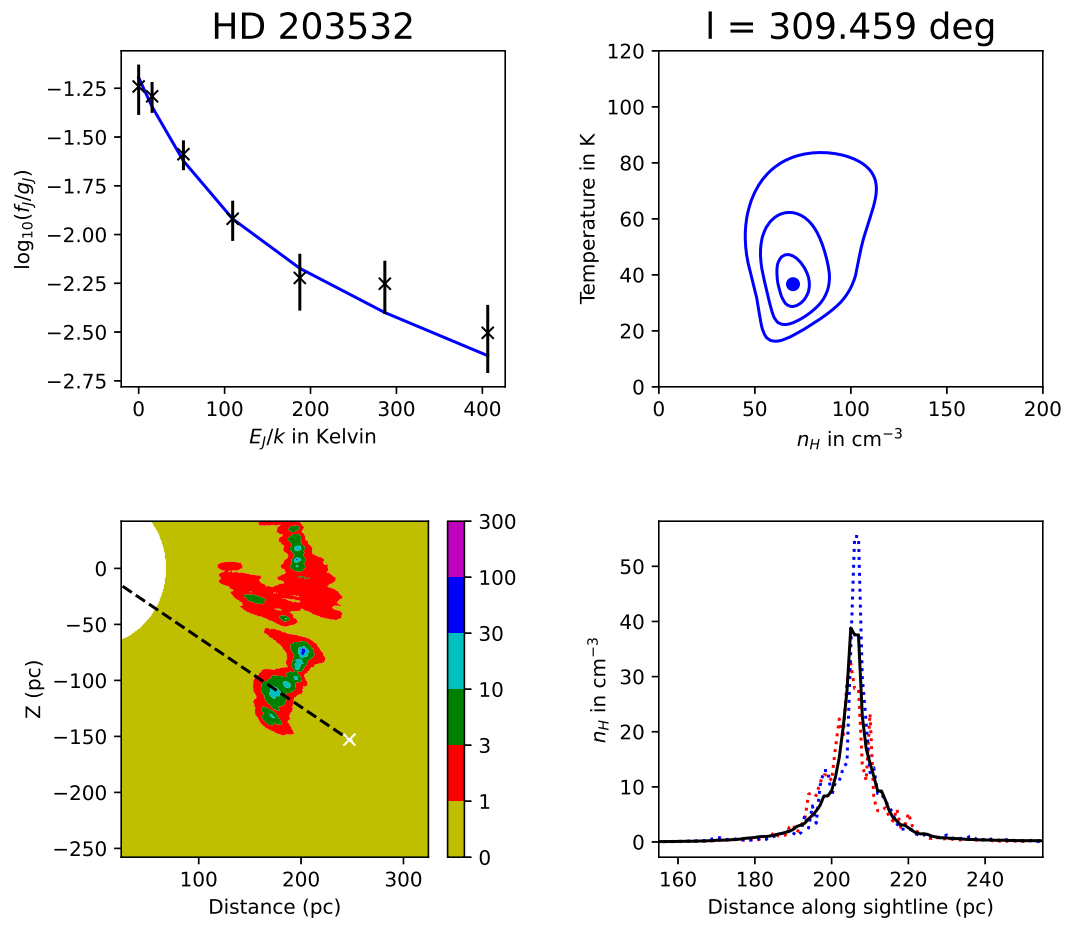


Figure 10.16. Results for the line-of-sight to HD 203532

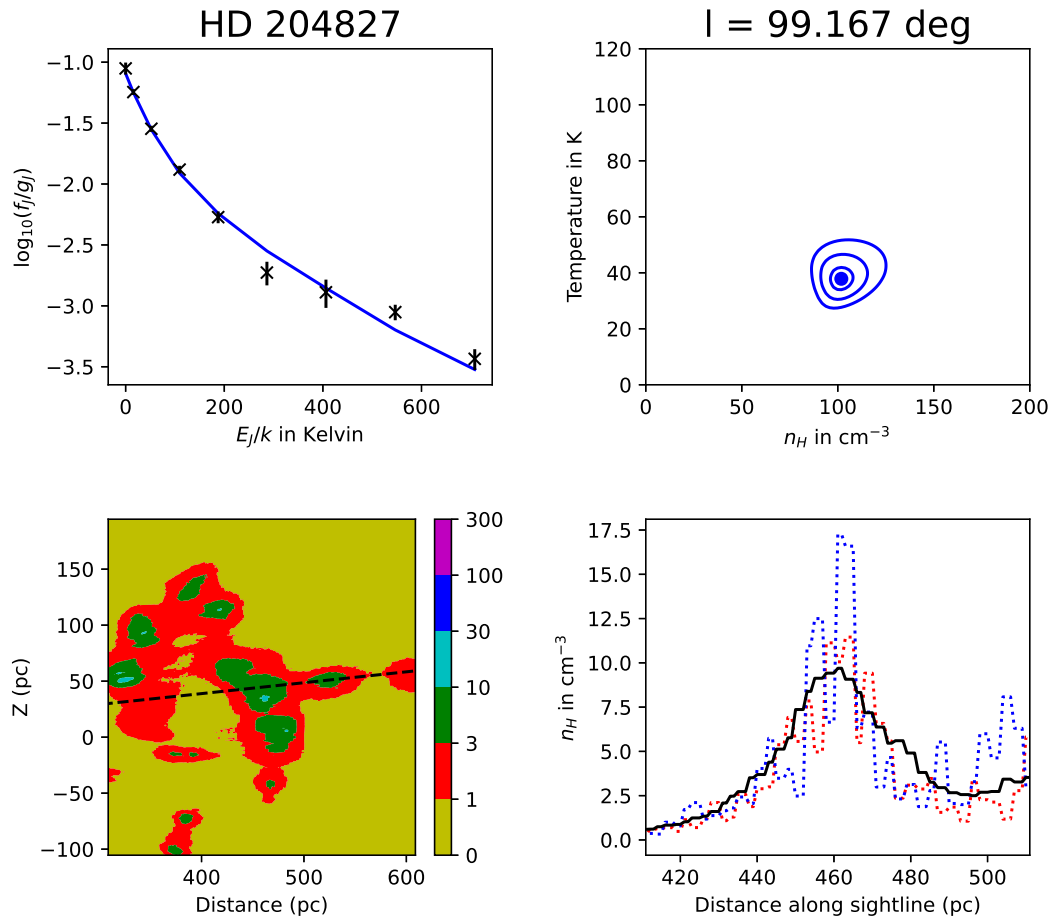


Figure 10.17. Results for the line-of-sight to HD 204827

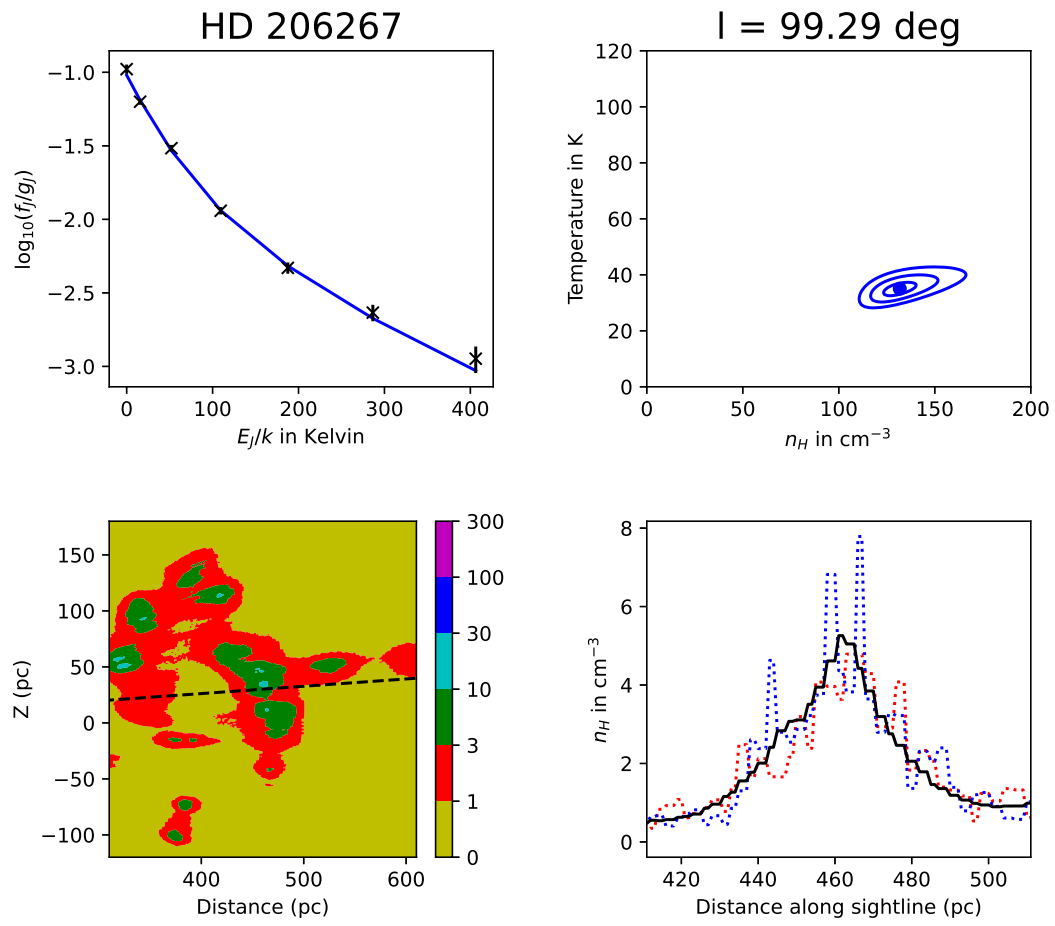


Figure 10.18. Results for the line-of-sight to HD 206267

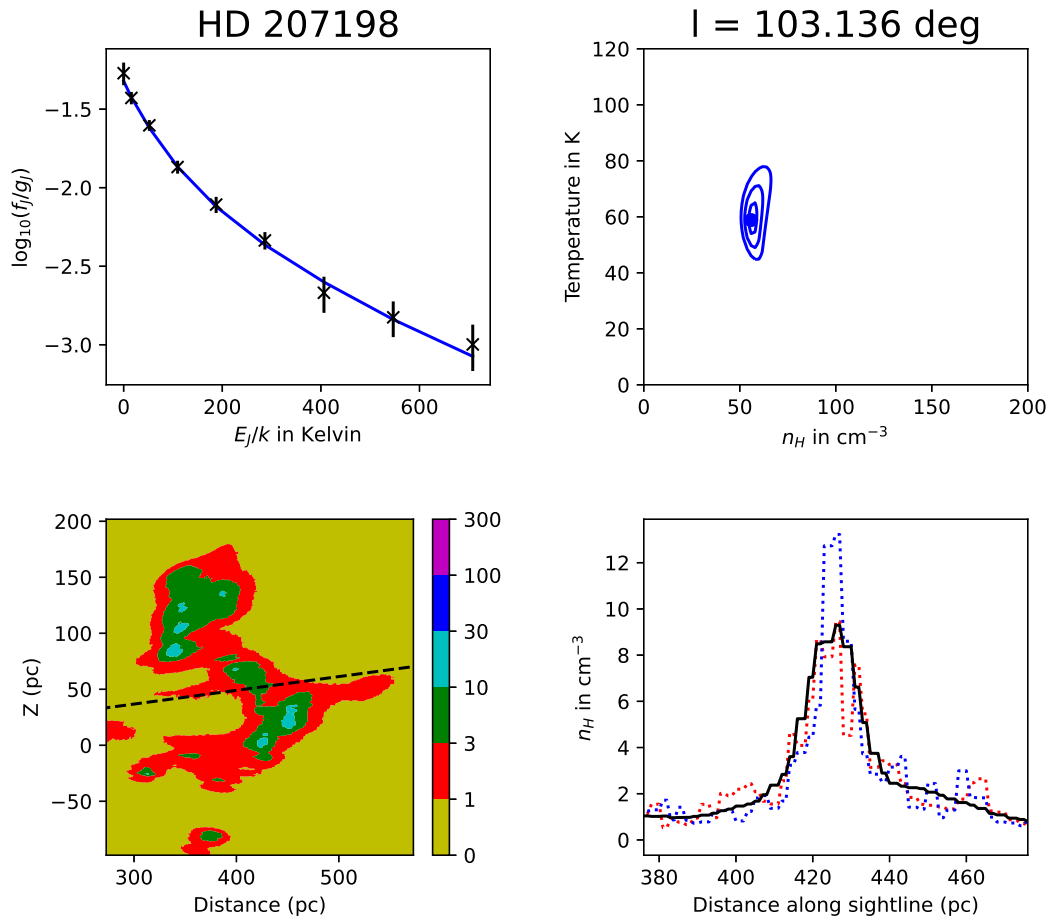


Figure 10.19. Results for the line-of-sight to HD 207198

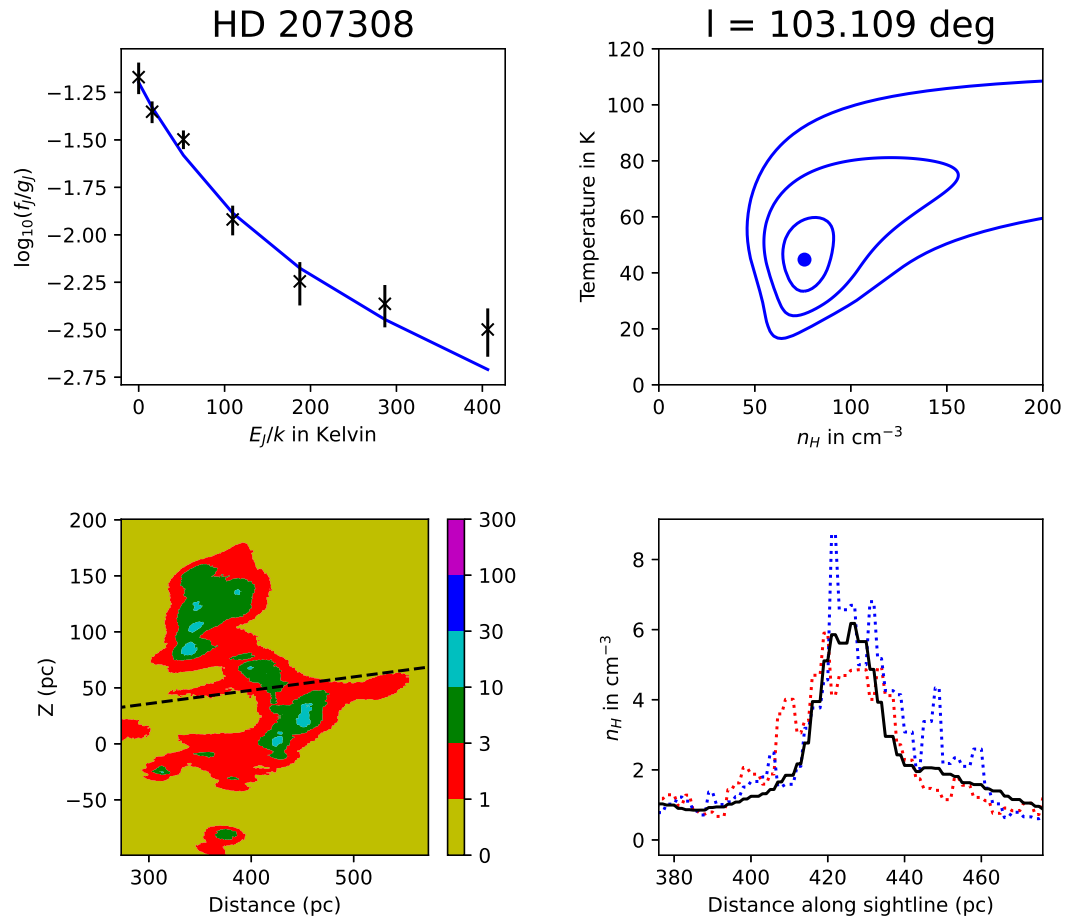


Figure 10.20. Results for the line-of-sight to HD 207308

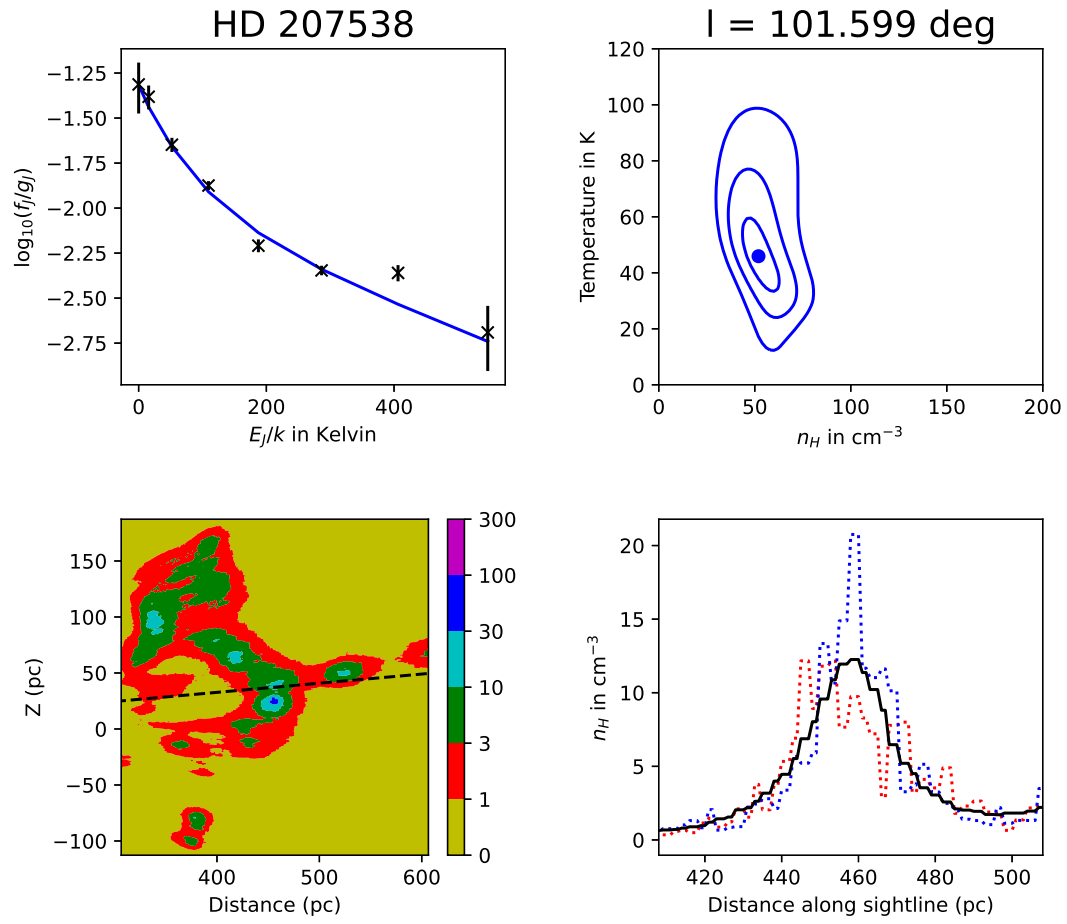


Figure 10.21. Results for the line-of-sight to HD 207538

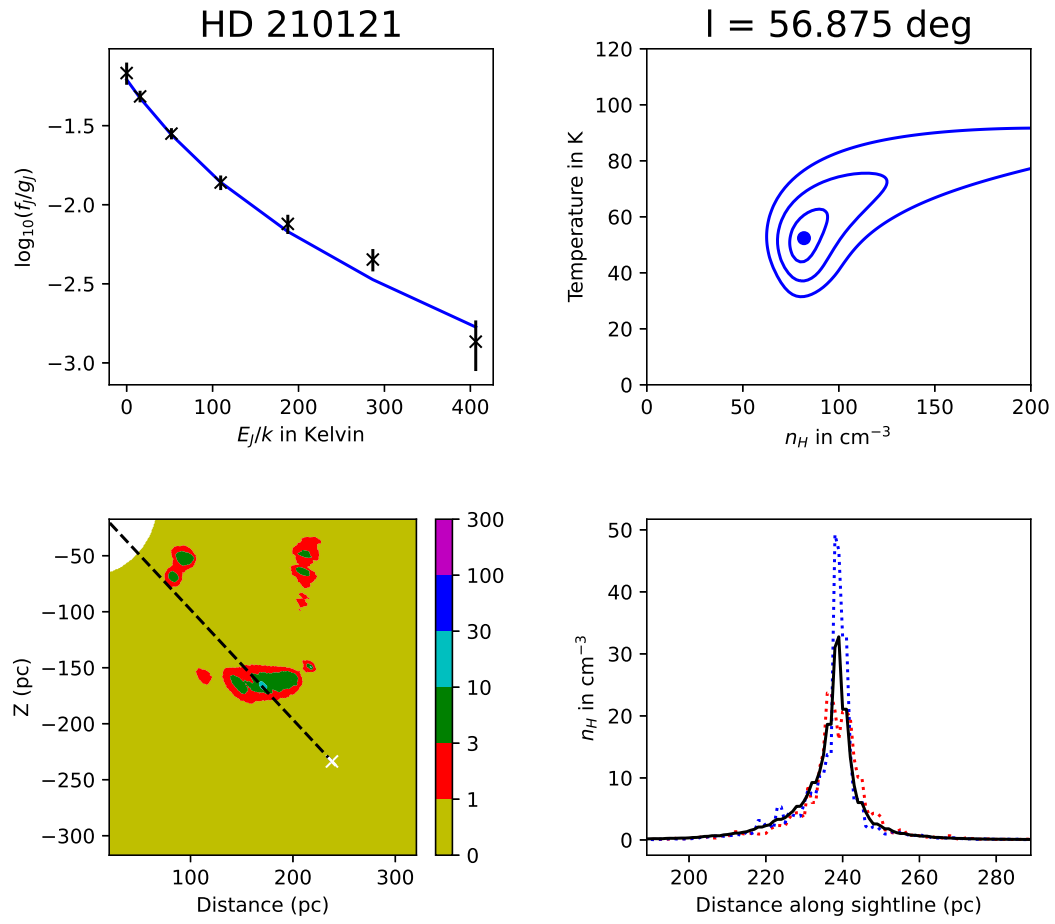


Figure 10.22. Results for the line-of-sight to HD 210121

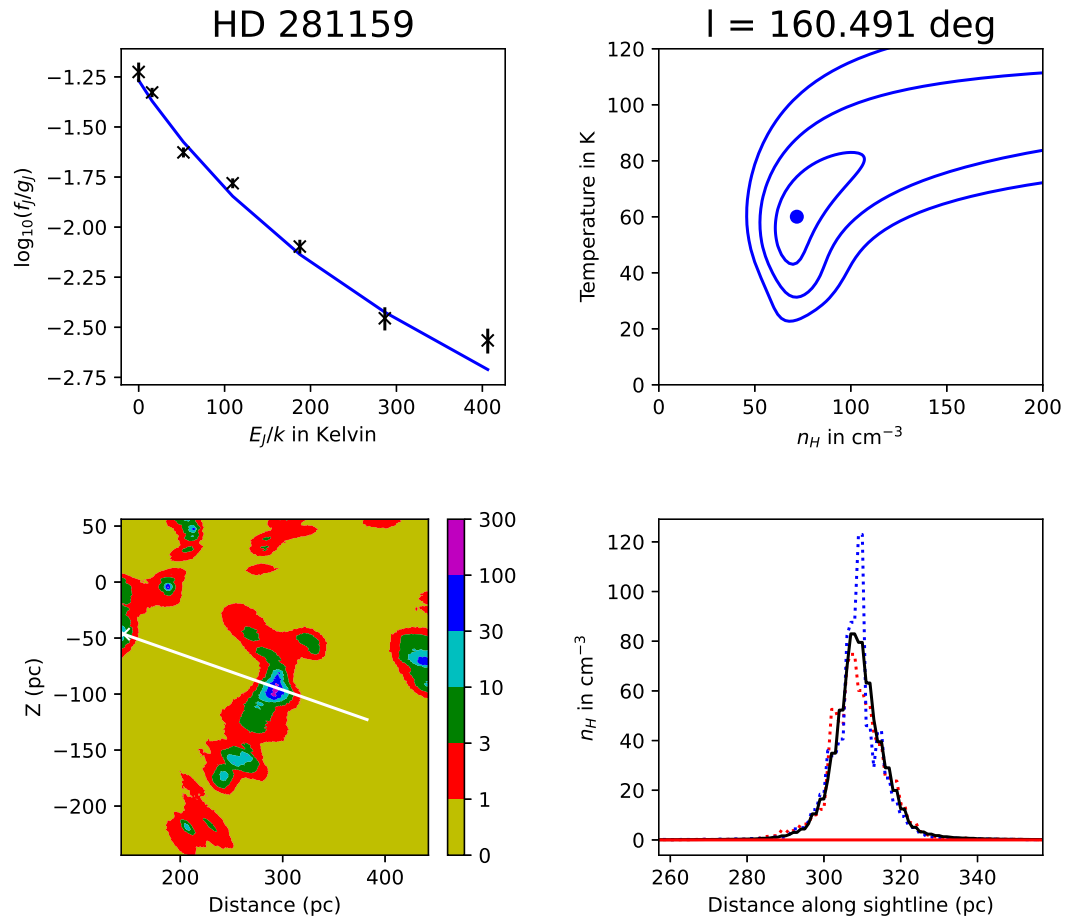


Figure 10.23. Results for the line-of-sight to HD 281159

REFERENCES

- Bohlin, R. C., Savage, B. D., & Drake, J. F. 1978, *ApJ*, 224, 132.
doi:10.1086/156357
- Casu, S. & Cecchi-Pestellini, C. 2012, *ApJ*, 749, 48.
doi:10.1088/0004-637X/749/1/48
- Chaffee, F. H., Lutz, B. L., Black, J. H., et al. 1980, *ApJ*, 236, 474.
doi:10.1086/157764
- Edenhofer, G., Zucker, C., Frank, P., et al. 2023, *arXiv:2308.01295*.
doi:10.48550/arXiv.2308.01295
- Fan, H., Rocha, C. M. R., Cordiner, M., et al. 2023, *arXiv:2310.03259*.
doi:10.48550/arXiv.2310.03259
- Federman, S. R. & Huntress, W. T. 1989, *ApJ*, 338, 140. doi:10.1086/167187
- Galazutdinov, G. A., Gnaciński, P., Han, I., et al. 2006, *A&A*, 447, 589.
doi:10.1051/0004-6361:20053410
- Gaia Collaboration 2020, *VizieR Online Data Catalog*, 1350
- Godard, B., Falgarone, E., & Pineau Des Forêts, G. 2009, *A&A*, 495, 847.
doi:10.1051/0004-6361:200810803
- Gredel, R. 1999, *A&A*, 351, 657
- Hauser, M. G., Arendt, R. G., Kelsall, T., et al. 1998, *ApJ*, 508, 25.
doi:10.1086/306379
- Hupe, R. C., Sheffer, Y., & Federman, S. R. 2012, *ApJ*, 761, 38.
doi:10.1088/0004-637X/761/1/38
- Iglesias-Groth, S. 2011, *MNRAS*, 411, 1857.
doi:10.1111/j.1365-2966.2010.17807.x
- Indriolo, N., Geballe, T. R., Oka, T., et al. 2007, *ApJ*, 671, 1736.
doi:10.1086/523036
- Indriolo, N. & McCall, B. J. 2012, *ApJ*, 745, 91.
doi:10.1088/0004-637X/745/1/91
- Jenkins, E. B. & Tripp, T. M. 2011, *ApJ*, 734, 65.
doi:10.1088/0004-637X/734/1/65
- Kaźmierczak, M., Schmidt, M. R., Bondar, A., et al. 2010, *MNRAS*, 402, 2548.
doi:10.1111/j.1365-2966.2009.16065.x
- Kaźmierczak, M., Gnaciński, P., Schmidt, M. R., et al. 2009, *A&A*, 498, 785.
doi:10.1051/0004-6361/200811558
- Lallement, R., Babusiaux, C., Vergely, J. L., et al. 2019, *A&A*, 625, A135.
doi:10.1051/0004-6361/201834695
- Leike, R. H., Glatzle, M., & Enßlin, T. A. 2020, *A&A*, 639, A138.
doi:10.1051/0004-6361/202038169
- McCall, B. J., Huneycutt, A. J., Saykally, R. J., et al. 2003, *Nature*, 422, 500.
doi:10.1038/nature01498
- Najar, F., Ben Abdallah, D., Jaidane, N., et al. 2008, *Chemical Physics Letters*, 460, 31. doi:10.1016/j.cplett.2008.05.070
- Najar, F., Ben Abdallah, D., Jaidane, N., et al. 2009, *JChPh*, 130, 204305.
doi:10.1063/1.3137583
- Najar, F. & Kalugina, Y. 2020, *RSC Advances*, 10, 8580.
doi:10.1039/C9RA10319H
- Neufeld, D. A. & Wolfire, M. G. 2017, *ApJ*, 845, 163.
doi:10.3847/1538-4357/aa6d68
- Obolentseva, M., Ivlev, A. V., Silsbee, K., Neufeld, D. A., Caselli, P., Edenhofer, G., Indriolo, N., Bisbas, T. G., and Lomeli, D. 2024, *ApJ*, submitted
- Phillips, T. R. 1994, *MNRAS*, 271, 827.
doi:10.1093/mnras/271.4.827
- Sembach, K. R., Danks, A. C., & Lambert, D. L. 1996, *ApJL*, 460, L61.
doi:10.1086/309971
- Sonnentrucker, P., Welty, D. E., Thorburn, J. A., et al. 2007, *ApJS*, 168, 58. doi:10.1086/508687
- Sternberg, A., Bialy, S., & Gurman, A. 2024, *ApJ*, 960, 8.
doi:10.3847/1538-4357/ad0465
- van Dishoeck, E. F. & Black, J. H. 1982, *ApJ*, 258, 533. doi:10.1086/160104
- van Dishoeck, E. F. & Black, J. H. 1986, *ApJS*, 62, 109. doi:10.1086/191135
- Welty, D. E., Sonnentrucker, P., Snow, T. P., et al. 2020, *ApJ*, 897, 36.
doi:10.3847/1538-4357/ab8f8e
- Zhang, X., Green, G. M., & Rix, H.-W. 2023, *MNRAS*, 524, 1855 (ZGR).
doi:10.1093/mnras/stad1941